

Understanding the Aeroacoustic Radiation Sources and  
Mechanism in High-Speed Jets

Dissertation

Presented in Partial Fulfillment of the Requirements for the Degree  
Doctor of Philosophy in the Graduate School of The Ohio State  
University

By

Michael Crawley, B.S.

Graduate Program in Department of Mechanical Engineering

The Ohio State University

2015

Dissertation Committee:

Dr. Mo Samimy, Advisor

Dr. Datta Gaitonde

Dr. James Gregory

Dr. Mei Zhuang

© Copyright by

Michael Crawley

2015

## **Abstract**

Who reads a dissertation abstract?

I would like to dedicate this work to Dr. Rachelle Speth, for her tireless efforts to  
convince me to hurry up and graduate already. Also, my parents.

## **Acknowledgments**

None. I did this entirely on my own.

## Vita

September 10, 1986 ..... Born - Plano, Texas

2009 ..... B.S. Mechanical Engineering,  
University of Texas, Austin.

2009-present ..... Graduate Research Associate,  
The Ohio State University.

## Publications

### Research Publications

**M. Crawley**, C.-W. Kuo, and M. Samimy, “Identification of the Acoustic Response in the Irrotational Near-field of an Excited Subsonic Jet.” submitted to *International Journal of Aeroacoustics*.

**M. Crawley**, R. Speth, D. V. Gaitonde, and M. Samimy, “A Study of the Noise Source Mechanisms in an Excited Mach 0.9 Jet - Complementary Experimental and Computational Analysis.” AIAA Paper 2015-0736, *53<sup>rd</sup> AIAA Aerospace Sciences Meeting*.

**M. Crawley**, A. Sinha, and M. Samimy, “Near-field and Acoustic Far-field Response of a High-Speed Jet Forced with Plasma Actuators.” *AIAA Journal*, expected 2015.

**M. Crawley** and M. Samimy, “Decomposition of the Near-Field Pressure in an Excited Subsonic Jet.” AIAA Paper 2014-2342, *20<sup>th</sup> AIAA/CEAS Aeroacoustics Conference*.

**M. Crawley**, A. Sinha, and M. Samimy, “Near-field Pressure and Far-field Acoustic Response of Forced High-Speed Jets.” AIAA Paper 2014-0527, *52<sup>nd</sup> AIAA Aerospace Sciences Meeting*.

**M. Crawley**, H. Alkandry, A. Sinha, and M. Samimy, “Correlation of Irrotational Near-Field Pressure and Far-Field Acoustic in Forced High-Speed Jets.” AIAA Paper 2013-2188, *19<sup>th</sup> AIAA/CEAS Aeroacoustics Conference*.

H. Alkandry, **M. Crawley**, A. Sinha, M. Kearney-Fischer, and M. Samimy, “An Investigation of the Irrotational Near Field of an Excited High-Speed Jet.” AIAA Paper 2013-0325, *51<sup>st</sup> AIAA Aerospace Sciences Meeting*.

**M. Crawley**, M. Kearney-Fischer, and M. Samimy, “Control of a Supersonic Rectangular Jet Using Plasma Actuators.” AIAA Paper 2012-2211, *18<sup>th</sup> AIAA/CEAS Aeroacoustics Conference*.

## Fields of Study

Major Field: Mechanical Engineering

Studies in: High-speed Jets, Aeroacoustics, Flow Control, Fluid Mechanics, Optical Diagnostics, Wavelets, Machine Learning

# Contents

	Page
Abstract . . . . .	ii
Dedication . . . . .	iii
Acknowledgments . . . . .	iv
Vita . . . . .	v
List of Figures . . . . .	ix
1. Introduction . . . . .	1
1.1 Motivation . . . . .	1
1.2 Background . . . . .	3
1.2.1 Flow Control . . . . .	3
1.2.2 Lighthill's Acoustic Analogy . . . . .	7
1.2.3 The Role of Large-Scale Structures . . . . .	10
2. Experimental Methodology . . . . .	14
2.1 Anechoic Chamber . . . . .	14
2.2 Localized Arc-Filament Plasma Actuators . . . . .	16
2.3 Data Acquisition . . . . .	17
2.3.1 Near- and Far-field Pressure . . . . .	17
2.3.2 Particle Image Velocimetry . . . . .	20
3. The Pressure Signature of Aeroacoustic Sources . . . . .	25
3.1 Preprocessing: Filtering the Actuator Self-Noise . . . . .	28
3.2 Acoustic/Hydrodynamic Decomposition . . . . .	31
3.2.1 The Wavelet Transform . . . . .	34

3.2.2	Validation . . . . .	38
3.3	Identifying the Acoustic Source Region . . . . .	46
4.	Estimation of Time-resolved Velocity Fields . . . . .	54
4.1	Stochastic Estimation . . . . .	55
4.1.1	Stochastic Estimation via Artificial Neural Networks . . . . .	57
4.1.2	Reduced-Order Representation of the Flow-Field . . . . .	61
4.2	Large-Scale Structure Interactions . . . . .	66
4.2.1	Global Flow-Field Effects . . . . .	66
5.	Dilatation as the Aeroacoustic Source . . . . .	70
5.1	Ribner's Acoustic Analogy . . . . .	71
5.2	Numerical Methodology . . . . .	72
5.3	Wavepackets in the Pseudo-Pressure Field . . . . .	85
6.	Conclusions . . . . .	87

## List of Figures

Figure	Page
1.1 Simplified diagram of jet noise sources, reprinted from Tam <i>et al.</i> [33].	12
2.1 Top-down view of anechoic chamber and free jet facility at GDTL; dimensions are in meters. . . . .	15
2.2 Photograph of anechoic chamber and nozzle, with near-field linear microphone array in foreground (a), schematic of all near-field microphone locations (b). . . . .	19
2.3 Schematic of synchronized PIV and near-field pressure data acquisition setup. . . . .	23
3.1 Phase-averaged waveforms along the first array position at $z/D = 3, r/D = 1.35$ (a) and a linear superposition of the phase-averaged waveform for the impulse excitation ( $St_{DF} = 0.05$ ) compared against periodic excitation ( $St_{DF} = 0.50$ ) (b). . . . .	26
3.2 Phase-averaged waveforms of the far-field at $30^\circ$ (a) and a linear superposition of the phase-averaged waveform for the impulse excitation ( $St_{DF} = 0.05$ ) compared against periodic excitation ( $St_{DF} = 0.25$ ) (b). . . . .	28
3.3 Schlieren image highlighting LAFPA compression waves. Reprinted from Samimy <i>et al.</i> [13]. . . . .	29
3.4 Raw and preprocessed near-field pressure. . . . .	30
3.5 Wavenumber-Frequency spectral energy. . . . .	33
3.6 Radial decay of the raw signal compared against the theoretically-obtained and experimentally-measured decay rates for the acoustic and hydrodynamic components. . . . .	39

3.7	Spectral comparison of decomposed hydrodynamic field compared against the raw near-field signal (a) and decomposed acoustic field compared against the far-field acoustic signal at $30^\circ$ . In both cases, the near-field signal was acquired at $z/D = 8, r/D = 2.2$ . . . . .	42
3.8	Wavelet power spectrum in the acoustic far-field at $30^\circ$ for the natural jet. . . . .	43
3.9	Comparison of phase-averaged waveforms produced by excitation at $St_{DF} = 0.05$ . As before, the near-field signal was acquired at $z/D = 8, r/D = 2.2$ . . . . .	44
3.10	Normalized two-point correlations for the natural jet between the near field and the far field at $30^\circ$ for two microphone array positions. . . . .	46
3.11	Normalized two-point correlations for the natural jet between the acoustic component of the near field and the far field at $30^\circ$ for microphone array position starting at $z/D = 1, r/D = 1.2$ . . . . .	49
3.12	Expected times of arrival for on-axis acoustic propagation, $\tau_a$ , and off-axis acoustic propagation, $\tau_s$ from a stationary source region centered at $x_s$ . . . . .	51
3.13	Normalized two-point correlations between the acoustic component of the near field and the far field at $30^\circ$ for microphone array position starting at $z/D = 1, r/D = 1.2$ for the natural jet (a), $St_{DF} = 0.05$ (b), $St_{DF} = 0.25$ (c) and $St_{DF} = 0.35$ (d). . . . .	52
4.1	Schematic of a feedforward ANN with a single hidden layer. The activation function is applied only to the hidden and output layers. The number of neurons depicted in each layer is meant to represent the <i>relative</i> number used by the actual ANN. . . . .	59
4.2	Comparison of a raw instantaneous axial velocity field $St_{DF} = 0.05$ (a) against the same velocity field estimated from the near-field pressure (b) and finally a reduced-order reconstruction of the raw velocity using the first 100 POD modes ; units are in m/s. . . . .	62
4.3	First 10 POD modes for $St_{DF} = 0.05$ , ordered top-down and then left-right. . . . .	64

4.4	First 10 POD modes for $St_{DF} = 0.25$ , ordered top-down and then left-right. . . . .	65
4.5	POD modal energy convergence. . . . .	66
4.6	Effect of excitation on the shear layer spreading rate, as visualized by the axial component of the velocity field. . . . .	68
4.7	Centerline Mach number for all excitation cases; baseline jet is indicated by ‘0.00’. . . . .	69
5.1	Two phases of actuation taken from the implicit LES database of Speth & Gaitonde [43]. Isosurfaces are computed from Q-criterion and colored by axial velocity, and the background corresponds to dilatation. . . . .	73
5.2	Streamwise velocity (a) and pressure (b) contours taken from the database of Speth & Gaitonde [43] for $St_{DF} = 0.05$ . . . . .	75
5.3	Azimuthal velocity at $z/D = 2.1$ for the same instance as the previous figure; units are in m/s. . . . .	76
5.4	Dilatation computed using only the axial and radial components (a) and computed using the full three-component velocity vector; a uniform colorscale has been used for the two plots. . . . .	77
5.5	Instantaneous axial (a,c,e) and radial (b,d,f) velocity components for the original (a,b), solenoidal (c,d), and potential (e,f) velocity fields (units in m/s), for $St_{DF} = 0.05$ . . . . .	81
5.6	Instantaneous pseudo-pressure field for the same conditions as Fig. 5.5. . . . .	83
5.7	Effects of filtering of the pseudo-pressure field on the calculated aeroacoustic source at $z/D = 1.75, r/D = 0.5$ ; amplitudes have been arbitrarily normalized to ease visual comparisons. . . . .	85
5.8	Instantaneous source field for the same conditions as Fig. 5.5. . . . .	86
5.9	??? . . . . .	86
5.10	??? . . . . .	86

# **Chapter 1: Introduction**

## **1.1 Motivation**

The advent of the turbojet engine led to a transformation in both commercial and military aviation, allowing for much faster flight than previously possible with propellor-driven aircraft. However, the increased thrust of turbojets has come at great cost; significant acoustic radiation is generated by the rotating components (compressor, turbine, fan), by the combustion process, and ultimately by the free jet itself. On the commercial side, the escalating number of flights, encroachment of urban and residential areas near airports, and tightening of environmental regulations have combined to force airports to institute curfews, surcharges and flight path restrictions to combat noise pollution. For the military, hearing damage inflicted on nearby personnel (particularly flight deck crew on aircraft carriers) has necessitated the implementation of noise reduction concepts on tactical aircraft. During takeoff and landing, when acoustic radiation is most problematic to ground crew and surrounding urban and residential areas, the dominant noise source of the jet engine is the aeroacoustic radiation generated by the high velocity engine exhaust. This has spurred extensive research, spanning over six decades, into the acoustic source mechanism in high speed, high Reynolds number jets.

While progress has been made in the field of aeroacoustics, both experimentally [1–3] as well as theoretically [4], understanding of jet noise sources and their radiation mechanisms remains incomplete [5]. This is due to the large number of interrelated parameters (e.g. Reynolds number, temperature ratio, acoustic Mach number, nozzle geometry, et cetera) as well as the large disparity in the associated length and time scales of the turbulent phenomena and the radiated noise. Simulations of controlled free shear layers have suggested that there is significant potential for noise reduction, on the order of 11 dB in some cases [6]. However, these simulations relied on non-physically defined actuation (that is, forcing was applied over a defined region by arbitrary energy, momentum, and body force terms), and a physical interpretation of the optimum forcing parameters was not immediately clear to the researchers. Current noise-mitigation technologies for free jets have largely been applied in an adhoc fashion, due to our incomplete understanding of the aeroacoustic sources. Fully realizing this maximum noise reduction potential will require a much more detailed understanding of the mechanism (or mechanisms) by which free jets radiate to the far-field.

It is generally agreed that the dominant noise sources are related to the large-scale turbulent structures present in the mixing layer of the jet. What remains to be determined is what aspects of the large-scale structure evolution and interactions are relevant to the noise generation process. Theoretical models of spatially- and temporally-modulated coherent structures have shown great promise in replicating the observed characteristics of the dominant far-field noise [7]. However, direct experimental data linking this structure evolution to the acoustic emission is still lacking. It is on this vein that the current work is focused. Until recently, experimental

data acquisition techniques have been unable to capture the flow physics with enough fidelity (lacking in either spatial or temporal resolution) in order to accurately model the large-scale structures and aeroacoustic sources. By combining contemporary data acquisition methods (free-field microphones and non-time-resolved particle image velocimetry) with novel post-processing algorithms this work aims to directly link the relevant vortex dynamics of the large-scale structures to the acoustic emission events, and in the process identify a simplified aeroacoustic source mechanism.

This study can be broken down into three distinct parts. In the first, the irrotational near-field and acoustic far-field of the jet is analyzed in order to identify the dominant acoustic source region. In the second, time-resolved velocity fields are estimated using an artificial neural network, which is trained to generate a mapping from time-resolved pressure measurements to instantaneous velocity. Lastly, the acoustic source is computed from the time-resolved velocity using Ribner's simplification of Lighthill's acoustic analogy.

## 1.2 Background

### 1.2.1 Flow Control

Controlling the development of the jet plume, and hence controlling the rate of mixing or intensity and characteristics of the emitted acoustic radiation, is a long running goal of the aeroacoustic community. Passive, permanent modifications to the nozzle have been shown to be quite adept at this task; some examples of these include tabs or chevrons [8]. These work to generate counter-rotating streamwise vortices in the developing shear layer, which serve to substantially increase mixing between the

core and coflow in the near-nozzle region and ultimately retard the growth of large-scale axisymmetric structures [9].

Unfortunately, these passive modifications have associated penalties to the engine performance, in terms of added weight or reduced thrust. Due to the passive nature of the flow modification, these performance penalties are in effect over the entire duration of the flight regardless of whether or not the noise reduction is needed. To improve engine efficiency, active control techniques are desired, since they can be activated when needed, such as during takeoff and landing, and deactivated when unneeded, such as after a commercial airliner reaches cruising altitude. Active control techniques, which seek to manipulate instabilities in the jet shear layer, have been extensively studied in low-speed, low-Reynolds number jets, the most common of which is acoustic drivers. However, as the speed and Reynolds number of the jet is increased (to match those in practical applications), so too does the required bandwidth and energy of the active drivers. Hence, acoustic or magneto-hydrodynamic drivers lose control authority in these regimes, and more powerful actuators are required.

The last decade has seen a rapid growth in the development of plasma actuators for use in high-speed flow control; though as of yet they have not progressed past the experimental phase. Localized arc filament plasma actuators (LAFPAs) are one such class of plasma actuator, which were developed by a collaboration between the Gas Dynamics and Turbulence Laboratory (GDTL) and the Non-Equilibrium Thermodynamics Laboratory (NETL) at the Ohio State University. LAFPAs can provide the high-amplitude and high-frequency excitation required for control of high Mach number and high Reynolds number jets [10]. GDTL has used these actuators for noise mitigation and flow control in Mach 0.9, Mach 1.3 and Mach 1.65 jets (both heated

and unheated) [11–16]. A review of the development of LAFPAs and their use in flow control and fluid phenomena research in high speed, high Reynolds number jets can be found in Samimy *et al.* [? ]. More recently, the diagnostic potential of LAFPAs for understanding jet flow phenomena has been explored. Excitation of instabilities in the flow by LAFPAs results in a definitive spatio-temporal origin to which resulting phenomena can be referenced. The absolute temporal reference afforded by LAFPA excitation provides researchers the ability to investigate the growth, saturation, and decay of structures with high fidelity. An example of their diagnostic potential can be found in the work of Kearney-Fischer *et al.* [17], which investigated Mach wave radiation from heated, high Mach number jets using schlieren imaging phase-locked to LAFPAs.

Unlike their passive counterparts (such as tabs or mechanical chevrons), or some other potential active flow control technologies (such as fluidic chevrons), LAFPAs control the shear layer development indirectly by exciting naturally occurring instabilities. The sharp velocity gradient in the jet shear layer (or, more precisely the inflection point produced by this sharp gradient) gives rise to the inviscid Kelvin-Helmholtz instability [18] (sometimes simply referred to as the initial shear layer instability). This instability is broadband and scales with the local momentum layer thickness and jet exit velocity ( $\theta/U_j$ ) ; perturbations over a wide range of frequencies can be amplified, though the dominant frequencies are found to be on the order of  $St_\theta = f\theta/U_j = 0.012$  for very thin boundary layers [19]. The Kelvin-Helmholtz instability then drives the development of the large-scale structures in the shear layer by amplifying fine-scale perturbations, ultimately causing them to roll-up into coherent structures regardless of Reynolds number [20, 21]. Owing to the axisymmetry of the

jet nozzle (i.e. that the initial shear layer wraps around and connects to itself), various azimuthal Fourier modes are unstable to perturbations (including both axisymmetric and higher order modes) [19].

The growth of the shear layer as it advects downstream ultimately dictates that the shear layer merges with itself; this location is referred to as the end of the potential core. A secondary instability, the jet column instability, manifests in axisymmetric jets and is related to the passage of large-scale structures through the end of the potential core. This instability scales with the jet exit diameter and jet exit velocity ( $D/U_j$ ) and is broadband, with a dominant characteristic frequency of  $St_D = fD/U_j = 0.3$ . The relation of the jet column instability to the initial shear layer instability is not well understood. Kibens argued that the jet preferred frequency is related to the initial shear layer frequency by the number of pairings of large scale structures that occur before the end of the potential core (i.e.  $f_n/f_p = 2^n$ ), as the frequency of the structures halves after each pairing process [22]. Conversely, Petersen claims that the jet preferred mode is simply the initial shear layer instability at the end of the potential core, and that the appearance of a single dominant lengthscale for the axisymmetric mode is due not to a type of ‘global’ instability of the flow field, but to a cutoff at the end of the potential core of the axisymmetric instability [23]. Regardless, it is clear that the large-scale oscillations of the jet shear layer and potential core are ultimately the product of small-scale perturbations which are amplified by the initial shear layer instability.

LAFPAs achieve flow control by utilizing this relationship between the initial shear layer instability and the jet column instability. The localized plasma arc-filament produces a rapid, localized heating through the Joule effect, and a compression wave

is formed [10]. Though these perturbations are spatially discrete, they quickly amplify into large-scale coherent structures with well-defined characteristic spatial, temporal, and azimuthal frequencies. Thus, LAFPAs are able to control the development of the most energetic scales in the jet shear layer; large-scale, azimuthally-coherent structures can be generated when enhanced mixing and jet spreading are desired, or smaller-scale, less azimuthally-coherent structures when noise reduction is necessary. In the present work, the subsonic jet is excited by LAFPAs, though here the goal is diagnostic rather than immediate practical application. The well-defined frequencies and phase of the large-scale structures produced by LAFPA actuation serve as an excellent reference for data acquisition and post-processing (e.g. phase-locking and phase-averaging).

### 1.2.2 Lighthill's Acoustic Analogy

Far outside the jet, where the medium is quiescent, no sources or sinks are present, and any disturbances are low-amplitude and isentropic, the governing equations can be linearized and simply reduced to a homogeneous wave equation

$$\frac{\partial^2 p}{\partial t^2} - c^2 \nabla^2 p = 0 \quad (1.1)$$

which describes the non-dispersive propagation of (acoustic) waves through space and time. Lighthill [24] was the first to identify that the governing equations for fluid dynamics could also be rearranged in such a manner as to produce a propagating wave equation *inside the jet*. Prior to this, aeroacoustic studies had observed that the frequency content of the far acoustic field matched that of the flow field, but had not identified a way to estimate the acoustic intensity.

Starting with the conservation of mass and momentum equations, one can take the divergence of the former and the partial derivative with respect to time of the latter, and combine these along with the equation of state to produce

$$\frac{1}{c^2} \frac{\partial^2 p}{\partial t^2} - \nabla^2 p = \nabla \cdot \nabla \cdot \mathbf{T}. \quad (1.2)$$

$\mathbf{T}$ , commonly referred to as *Lighthill's stress tensor*, comprises Reynolds stresses, viscous stresses, and entropy fluctuations, respectively:

$$\mathbf{T} = \rho \mathbf{u} \otimes \mathbf{u} - \tau + \mathbf{I} [(p - \bar{p}) - c^2(\rho - \bar{\rho})]. \quad (1.3)$$

Here,  $c$  refers to the ambient speed of sound,  $\mathbf{I}$  is the identity matrix,  $\tau$  is the shear stress tensor, and an overbar ( $\bar{\cdot}$ ) corresponds to a time-averaged quantity. This transformation has the effect of approximating the real system as a uniform acoustic medium at rest which is being driven by an external fluctuating force field. As the wave operator is linear, the solution to this equation can be formulated with the aid of Green's functions,

$$\frac{\partial^2 G}{\partial t^2} - c^2 \nabla^2 G = \delta(\tau - t) \delta(\mathbf{x}' - \mathbf{x}). \quad (1.4)$$

The solution to this (see Crighton *et al.* [25]) is the deceptively simple spatial integration of the source field at retarded time (that is, it is accounting for the propagation delay from the source location to the observer):

$$p(\mathbf{x}, t) = \frac{1}{4\pi c^2} \nabla \cdot \nabla \cdot \int_{\Omega} \frac{\mathbf{T}(\mathbf{x}', t - |\mathbf{x} - \mathbf{x}'|/c)}{|\mathbf{x} - \mathbf{x}'|} d^3 \mathbf{x}'. \quad (1.5)$$

Lighthill's derivation of what became known as the first acoustic analogy (which in fact was specifically tailored to the study of jet noise) reformed the study of aeroacoustics. As has been discussed by many authors before (see Goldstein [26] for example),

this equation describes the propagation of sound, through a quiescent medium, generated by quadrupole sources. There have been several major assumptions made in this derivation, that the flow is completely subsonic (and hence no shock or expansion waves are present), that the observer location is far from the jet (and hence hydrodynamic pressure fluctuations or ‘pseudo-sound’ is negligible), that there are no solid boundaries near the flow (and hence, no reflections, diffraction, absorption, or scattering) and finally that the acoustic waves themselves do not act as sources as they propagate through the flow. Nonetheless, this theoretical framework is still applicable to a wide variety of commercial and scientific inquiries, present study included.

Theoretical work based on Lighthill’s approach was successful in predicting some aspects of experimentally-observed jet noise. Namely, stochastic source models of quadrupoles (per the aeroacoustic community’s understanding of jet turbulence at the time) predicted a far-field pressure intensity scaling of  $I \sim U_j^8$  which agreed with experimental results from cold, subsonic jets at sideline angles [2]. However, this scaling law does not hold when the jet is heated, necessitating more complex source models. Unfortunately, given the complexity of the source field, even modern experimental techniques cannot acquire the full source with sufficient spatial and temporal fidelity to elucidate the flow structures responsible for the dominant noise emission.

Later researchers further refined Lighthill’s approach (e.g. Howe [? ], Goldstein [26] and Lilley [27]); providing successively clearer characterizations of the source physics. In addition to the true noise sources, Lighthill’s acoustic source term includes flow-acoustic interactions, which describe diffraction and convection effects rather than true sources of noise, and which these researchers have attempted to separate

from the true noise sources. Alternative acoustic analogies have also been proposed, such as Powell's theory of vortex sound [28] and Doak's momentum potential theory [29]. In a slightly different vein, analytical decompositions have been performed in order to separate the disparate fluid phenomena inherent in Lighthill's source term and identify the roles of each [4]. In each of these theories however, the source field for a high-speed, turbulent jet is highly complex and defies a simple physical understanding of the dynamical processes which lead to the noise emission.

### 1.2.3 The Role of Large-Scale Structures

Initial understanding of turbulence was that it was stochastic in nature - that the frequency and appearance of turbulent eddies in a flow was random, with little to no prescribed preference. It was in this context that Lighthill's acoustic analogy was first developed, and as a result initial models for the source field assumed a stochastic distribution of quadrupoles. This source model was shown to produce an intensity which scaled with the eighth-power of the flow velocity, which was in general agreement with the experimentally-observed intensity scaling of cold, subsonic jets [30]. The downstream convection of these quadrupoles produces a preferential directivity in the emitted acoustic radiation, with a maximum predicted to occur near  $45^\circ$  from the jet axis, again in general agreement of experimental far-field spectra [30]. However, researchers have found that stochastic quadrupole source models fail to accurately predict the intensity scaling of jet noise in heated jets or cold jets at low observer angles [1]. As Lighthill's analogy is an exact rearrangement of the governing equations (aside from the relatively minor assumption of a constant speed of sound), the error lies in our understanding of the aeroacoustic source.

Mollo-Christensen [31], and later Crow & Champagne [20] and Brown & Roshko [21], were the first to identified large-scale, coherent vortical structures underpinning turbulent free shear layers, in addition to the fine-scale, stochastic eddies. Later researchers linked the appearance of these large-scale structures to natural flow instabilities (predominantly the Kelvin-Helmholtz instability discussed in §1.2.1) [18, 19, 32]. Following the identification these coherent structures in turbulent jet shear layers, source term models based on large-scale eddies have frequently been employed, to varying degrees of success.

A simplified model of the noise generation process in stationary free jets can be found in Fig. 1.1. This model is from the work of Tam *et al.* [1, 3], who observed that the far-field spectra could be represented as a combination of two similarity spectra based on polar angle of the observer, regardless of jet Mach number or temperature. At observer angles close to the jet downstream axis, the spectra exhibited a clearly defined spectral peak ( $F$ -spectrum), whereas at sideline or upstream angles the spectra were broadband ( $G$ -spectrum). From this observation the two-component acoustic source model was born: the isotropic fine-scale turbulence, dominant in the near-nozzle region, is responsible for the omni-directional acoustic radiation that dominates the sideline and upstream polar angles. On the other hand, the large-scale turbulent structures which exist further downstream produce the superdirective radiation that is readily apparent at aft polar angles. This model of large-scale (and to a lesser extent fine-scale) turbulence noise generation explains the so-called 'mixing noise' generated by both subsonic and supersonic jets. Numerous experimental studies have lent credibility to this view of aeroacoustic noise generation; see for example, Panda *et al.* [34], Viswanathan *et al.* [35], Tam *et al.* [3], and Bogey & Bailley [36].

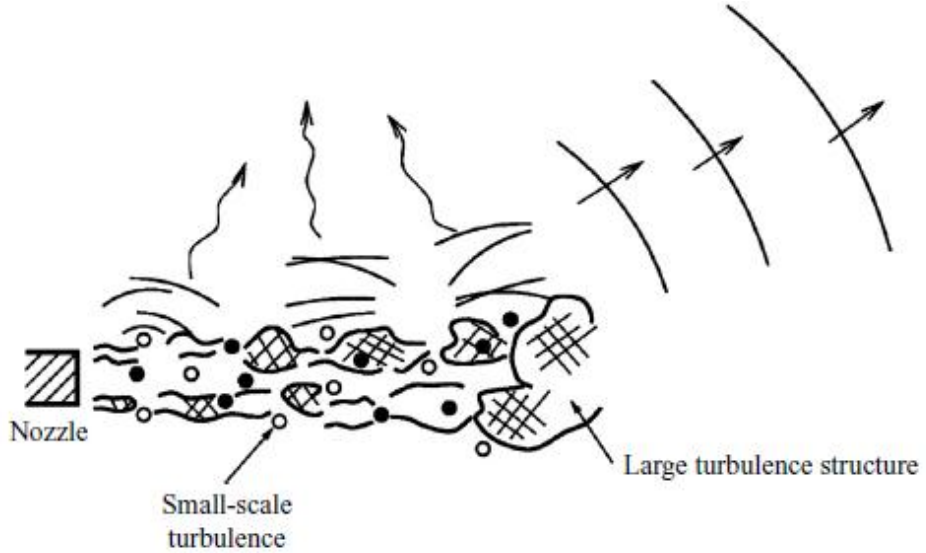


Figure 1.1: Simplified diagram of jet noise sources, reprinted from Tam *et al.* [33].

There is little disagreement at this point that the large-scale coherent structures in the turbulent shear layer are responsible for the dominant noise emission; however, the exact dynamics of these which leads to acoustic emission are as of yet still not well-understood.

As discussed by Tam *et al.* [37] (among many others), large-scale structures can be represented as instability waves superimposed upon the mean flow. At subsonic convection velocities, a plane instability wave with fixed frequency-wavenumber will emit no acoustic radiation to the far-field. However, modulation of the instability wave's amplitude creates a dispersion in the energy content of the instability wave. By doing so, the broadband instability wave, now commonly referred to as a *wavepacket*, can shift energy to supersonic phase-velocities and hence produce sound. Wavepacket models for noise emission have become commonplace, owing to their great success at predicting low-angle acoustic emission [38]. Simple linear wavepacket models have

allowed researchers to probe different aspects of the waveform modulation, in turn illuminating possible relevant dynamical behavior of the large-scale structures for the noise generation process. Temporal modulation of the wavepacket's amplitude and spatial extent (termed ‘jittering’ by the researchers) were shown to increase the efficiency of the noise source [7]; this conforms to experimental results which have indicated that the noise generation in free jets is highly intermittent [? ? ]. Though progress has been made in experimentally measuring wavepacket characteristics in high-speed turbulent jets [39, 40], a direct link between large-scale structure dynamics and the aeroacoustic source has remained elusive.

As a side note, additional noise source mechanisms have been identified for supersonic jets. In imperfectly expanded jets, shock cells are produced in the jet. As turbulent structures pass through these waves, the sharp pressure gradients cause them to emit acoustic radiation. This is observed directly in the far-field as a broad-band amplification at high frequencies, referred to simply as broad-band shock-associated noise (BBSAN). In stationary or subsonic airframes this radiation can generate a feedback loop, whereby the noise travels upstream to the nozzle exit, excites the initial shear layer, and produces new structures at the same frequency. A high-amplitude, narrow-band tone (screech noise) is the end result of this feedback loop. Lastly, supersonically-convectiong (relative to the ambient) large-scale structures (which exist in supersonic and heated jets) produce high-amplitude, strongly-directional acoustic radiation towards aft angles. This Mach wave radiation can be explained by a wavy-wall analogy [37]. In the present work, the jet is unheated and subsonic; as such these noise sources are not present and therefore neglected throughout the rest of this work.

## Chapter 2: Experimental Methodology

### 2.1 Anechoic Chamber

All experiments were conducted at the GDTL within the Aerospace Research Center at the Ohio State University. Compressed, dried, and filtered air is supplied to the facility from two cylindrical storage tanks with a total capacity of 43 m<sup>3</sup> and maximum storage pressure of 16 MPa. The air may be routed through a storage heater, which allows the jet to operate with a stagnation temperature up to 500 °C, before expanding through a nozzle and exhausting horizontally into an anechoic chamber. As the current work was focused on a cold jet, the heater was rarely necessary; in certain circumstances though (namely, long experimental runs) the storage heater and bandheaters were used to slightly preheat the flow, thereby mitigating the temperature drop as the storage tanks were drained of high-pressure air. Opposite the nozzle, a collector accumulates the jet and entrained air and exhausts to the outdoors. A schematic of the anechoic chamber can be seen in Fig. 2.1. The dimensions of the chamber are 6.20 m wide by 5.59 m long and 3.36 m tall, with internal wedge-tip to wedge-tip dimensions of 5.14 m by 4.48 m and 2.53 m, respectively. The design of the chamber produces a cutoff frequency of 160 Hz, below the frequencies of interest for

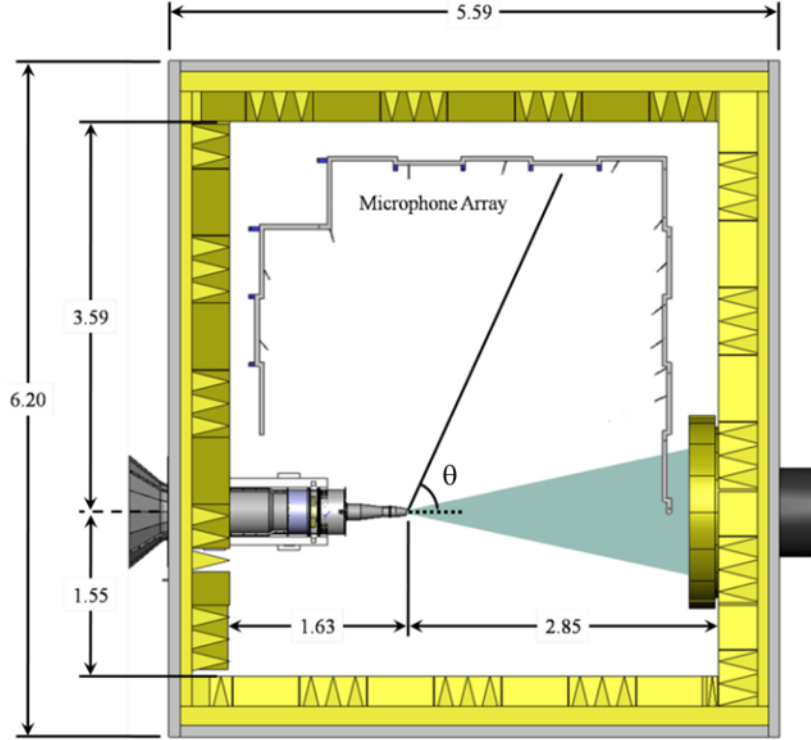


Figure 2.1: Top-down view of anechoic chamber and free jet facility at GDTL; dimensions are in meters.

this study. A more detailed description of the GDTL anechoic chamber properties and validation has been given by Hahn [? ].

For this study a converging, axisymmetric nozzle with exit diameter  $D$  of 25.4 mm was used. The internal contour of the nozzle was designed using a fifth order polynomial. The nozzle utilized a thick-lipped design in order to simplify the mounts for the LAFPA extension, which housed the eight actuators used in this study. For the experiments reported in this paper, the jet was operated at a Mach number ( $M_j$ ) of 0.90, and with a total temperature ratio of approximately unity. The Reynolds number based on the jet exit diameter was  $6.2 \times 10^5$ ; previous investigations using

hot-wire anemometry have indicated that the initial shear layer is turbulent for this operating condition with momentum thickness 0.09 mm and boundary layer thickness 1 mm [16].

## 2.2 Localized Arc-Filament Plasma Actuators

The design of the localized arc-filament plasma actuators, as well as the driving circuitry, has undergone a slow evolution since their initial development by the GDTL and NETL. In the current work, each LAFPA actuator consists of a pair of 1 mm diameter tungsten pin electrodes. The center-to-center spacing between electrode pairs for each actuator is 4 mm. Eight actuators were uniformly spaced around the nozzle perimeter 1 mm upstream of the nozzle exit. For electrical and thermal durability, the electrodes were housed in a boron nitride (grade AX05) extension attached to the end of the nozzle. A groove with dimensions of 1 mm wide and 0.5 mm deep is machined in the boron nitride, into which the electrode tips protrude, to provide a region of low momentum flow in order to stabilize the plasma arcs. It has been shown that the existence of this groove does not substantially alter the flow field or the control authority of the LAFPAs [Hahn]. A detailed description of initial development and LAFPA characteristics can be found in Utkin *et al.* [10].

The LAFPAs were energized by a multi-channel, high-voltage plasma power generator capable of simultaneously powering up to eight LAFPAs, which was designed and built in-house at the GDTL. In this second-generation power supply, each individual circuit consists of a switchable capacitor in line with a high voltage transformer; the arcing electrodes are connected to the secondary side of the coil. The capacitor is charged by a 100 V DC power supply when the first switch is closed and the second is

opened; at the user-specified time the switches flip and it discharges through the coil. The switches are controlled by a 16-channel digital I/O card and National Instruments' Labview software, operated by a dedicated computer. The plasma generator provides independent control of the frequency, duty cycle/pulse width, and phase of each individual actuator (though not the amplitude). The pulse width was held constant at 7 s, which was found to be the minimum pulse width at which the actuators consistently arced for all frequencies explored in this study [citation]. The circuit is limited to 20 kHz due to thermal concerns. However, as the current work is focused on the evolution of large-scale structures (and ultimately their acoustic radiation), for which the dominant frequencies are on the order of 3 kHz, this is not an issue.

## 2.3 Data Acquisition

### 2.3.1 Near- and Far-field Pressure

Near-field and far-field pressure measurements were acquired using Brüel & Kjær 0.25-inch 4939 microphones and preamplifiers. The signal from each microphone is band-pass filtered from 20 Hz to 100 kHz using a Brüel & Kjær Nexus 2690 conditioning amplifier, and recorded using National Instruments PXI-6133 A/D boards and LabVIEW software. The microphones are calibrated using a Brüel & Kjær 114 dB, 1 kHz sine wave generator (type 4231). The frequency response of the microphones is flat up to roughly 80 kHz, with the protective grid covers removed.

Far-field acoustic pressure is acquired at three polar angles: 30, 60 and 90, as measured from the downstream jet axis. The positioning of the far-field microphone array can be seen in Fig. 2.1. The microphones were oriented such that they are at

normal incidence to the jet downstream axis at the nozzle exit. The radial distance of the microphones ranges from 101D at 30 to 145D at 60.

The near-field pressure was acquired during two separate experimental campaigns; the first focusing purely on the near-field and far-field pressure and the second focusing on the instantaneous velocity field. During the first campaign, the irrotational near-field was acquired using a linear array of sixteen microphones located along the meridional plane of the jet; the spacing varied along the array from 1D to 2D (see Fig. 2.2). The array was mounted on a two-axis linear traverse system the array and was inclined at an angle of  $8.6^\circ$  to the jet axis in order to match the spreading angle of the jet shear layer, as determined via PIV measurements during previous studies [28]. The traverse was controlled using LabView and enabled the acquisition of pressure measurements at various radial positions with respect to the jet axis. Initially, the most upstream microphone is positioned at  $x/D = 1$  and  $r/D = 1.20$ , which is just outside the initial shear layer. For subsequent cases, the microphone array was incremented radially outward by 0.5D for a total travel distance of 7D, for a total of 15 array locations in the radial direction. Voltage signals were collected at 200 kHz with 81920 data points per block; sub-blocks of 8192 data points were used when calculating short-time power spectral densities, resulting in a frequency resolution of 24.4 Hz. Ten blocks were recorded for each case resulting in four seconds of data, which has been found to be sufficient for statistical convergence.

In the second experimental campaign, a shorter array consisting of 12 microphones equally space by 1D was used. In this case, the array was mounted from the floor and at an angle off the meridional plane of the jet (with microphone tips angled

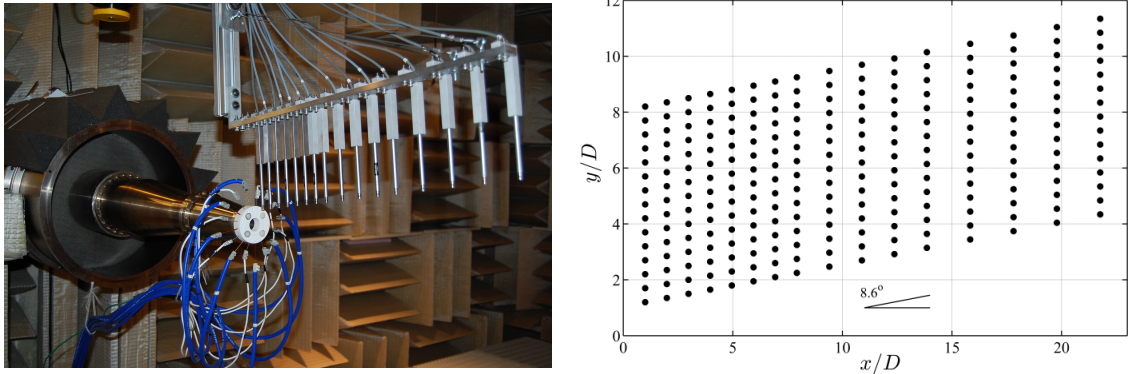


Figure 2.2: Photograph of anechoic chamber and nozzle, with near-field linear microphone array in foreground (a), schematic of all near-field microphone locations (b).

normal to the jet axis). This setup was used in conjunction with the particle image velocimetry described in the following section; the microphone array was placed off of the meridional plane so that it did not intersect with the laser sheet. As before, the microphone array was angled  $8.6^\circ$  with respect to the jet axis in order to match the spreading rate of the shear layer, and the axial and radial position was set to match the closest microphone array location used during the first experimental campaign. Voltage traces were acquired at 400 kHz, with 24576 points collected per block. The voltage traces were collected simultaneously with streamwise particle image velocimetry measurements; 1500 blocks were acquired, corresponding to the 1500 acquired images.

In addition to the microphone voltage traces, the acoustics data acquisition system recorded a reference signal corresponding to the LAFPA excitation. The TTL pulse sequence, which controls the LAFPAs, was supplied to an Agilent 3320A waveform generator. The rising edge of the TTL pulse triggered a sharp drop in the output

voltage of the waveform generator, which then ramps back up to the original voltage over a time interval which is shorter than the minimum excitation period. The output from the waveform generator was acquired simultaneously with the near- and far-field pressure signals using the aforementioned National Instruments hardware and software. As the excitation frequency, azimuthal mode, and ramp signal are well defined, this system enables the identification of the zero phase of actuation and hence, the ability to phase-average the pressure signals over the excitation period, akin to the work performed in Sinha *et al.* [? ]. This ensures that the seeded perturbations can be readily identified in the noisy flow, as well as allowing pressure signals, which were not recorded simultaneously (i.e. different near-field array positions), to be analyzed concurrently.

### 2.3.2 Particle Image Velocimetry

The instantaneous velocity was acquired using streamwise, two-component particle image velocimetry (PIV). A Spectra Physics, double-pulsed Nd:YAG laser (model PIV-400) was used as the illumination source. Due to facility requirements, the laser was located on a vibrationally-damped table outside the anechoic chamber and the laser beam was routed into the chamber using an overhead port; this resulted in a beampath of  $\sim 10$  m. The laser sheet was formed using two cylindrical and one spherical lens; one of the cylindrical lenses was mounted to a rotational stage in order to ensure that the final laser sheet was normal to the jet exit (i.e. the laser sheet was streamwise to the jet). Alignment of the separate laser heads was initially performed using burn paper; final alignment was performed by seeding a low-velocity flow and visually checking that the same particles were captured in both frames. Per the best

practices explained in the LaVision DaVis manual, the timing between the two laser pulses was set so that particles in the jet core translated downstream by roughly half of the minimum correlation window width (16 pixels). For the present work, this resulted in a time delay of  $3 \mu\text{s}$ . It was later observed that the actual time delay produced by the laser did not match the delay specified in the control software; this resulted in incorrect velocities being computed by the cross-correlations. In order to correct for this, the laser pulses were recorded using a ThorLabs DET210 photodetector and a LeCroy Wavejet 324A oscilloscope; the final vector fields were linearly scaled based on the ratio between the specified time delay and the measured time delay.

The jet core was seeded using Di-Ethyl-Hexyl-Sebacat (DEHS); the oil was atomized using a LaVision Aerosol generator and injected upstream of the turbulence screens in the stagnation chamber in order to produce a uniform seed particle density. As the jet entrains a significant amount of the surrounding ambient fluid as it evolves downstream, the coflow around the jet must also be seeded in order to accurately measure the outer shear layer velocity. For this, a TSI 6-jet atomizer (model 9306A) and olive oil was used; injection occurred into a plenum which surrounded the core stagnation chamber. Per the manufacturer's specifications, both atomizers provided nominally sub-micron seed particles. To ensure consistent seeding, this coflow was driven using a small Aerovent blower and a series of high-pressure ejectors. As a result, for the PIV data acquisitions, the jet core was surrounded by a  $\sim 5 \text{ m/s}$  coflow.

Image groups were acquired using two LaVision Imager Pro SX 5M cameras, which had 12-bit resolution and  $2560 \times 2180$  pixels. The combination of the PIV-400 laser and the Imager Pro SX cameras resulted in a maximum acquisition rate for the image

groups of 5 Hz. Nikon Nikkor 105 mm f/1.8 lenses were used, and 532 nm bandpass filters were mounted on the lenses. The cameras were positioned such that they were nominally normal to the image plane, negating the need for scheimpflug mounts. This was done as having high spatial resolution and field of view were deemed to be more important than having full, three-component velocity vectors. The cameras were aligned such that there was roughly a 10% overlap between the two images. This setup is generally designated as “side-to-side” in order to differentiate it from stereoscopic PIV; a schematic of the setup can be found in Fig. 2.3. The cameras were calibrated simultaneously using a LaVision calibration plate (type 31). Hardware background subtraction was used in order to reduce the effect of reflections off of the nozzle extension and near-field microphone array.

The image groups were acquired in two modes: ensemble and phase-locked. When in phase-locked mode, a reference signal from the LAFPA control computer was used as an external trigger for LaVision’s DaVis software; various filters were placed inline in order to damp the electromagnetic interference generated by the LAFPAs. The reference signal was downsampled to roughly 10 Hz by the LAFPA control computer, and delayed appropriately in time to control the acquired actuation phase. For this case, 300 image groups were acquired for an individual phase. In ensemble mode, image groups were acquired randomly in time at the system’s maximum acquisition rate (5 Hz). In this case, the PIV computer was set to output a reference signal which was used to trigger the acoustics data acquisition system. The timing was set such that the PIV image acquisition would occur roughly in the center of a data block acquired by the acoustics system; the signal from a ThorLabs DET210 photoreceiver was also recorded in order to accurately identify the timing of the image acquisition

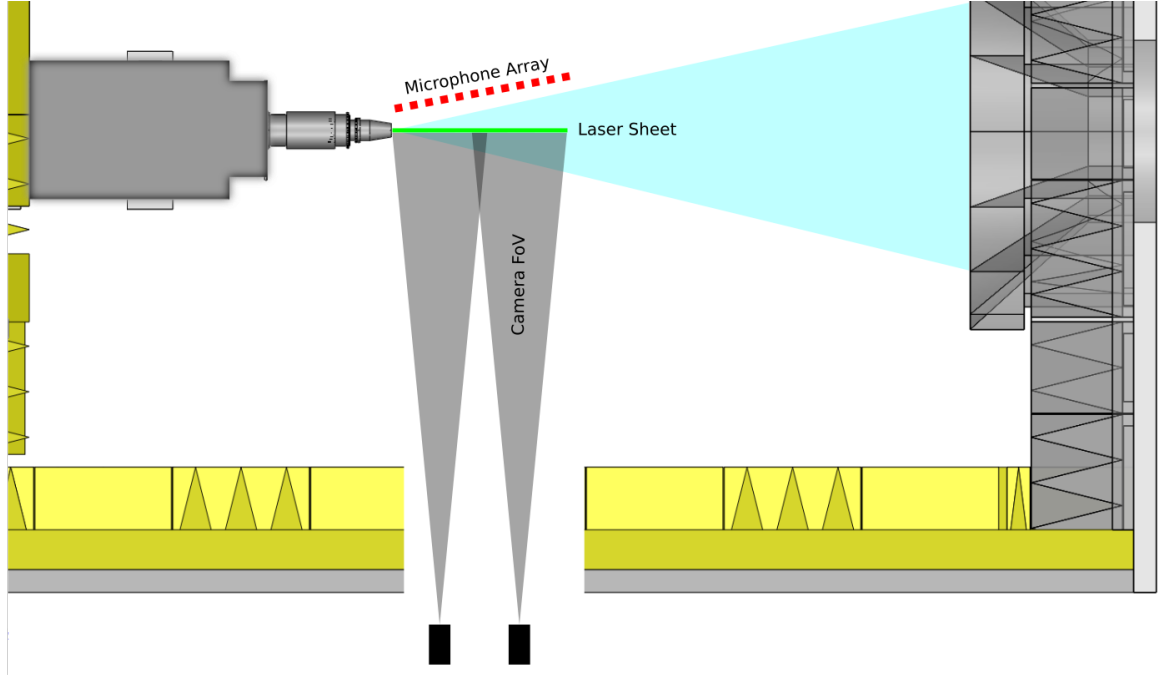


Figure 2.3: Schematic of synchronized PIV and near-field pressure data acquisition setup.

in relation to the pressure time traces. For this case, 1500 image groups were acquired for each case.

Instantaneous velocity vectors were computed using LaVision’s DaVis software. Multipass, FFT-based cross-correlations were used, with decreasing window size ( $64 \times 64$  for the initial pass, and  $32 \times 32$  for the final three passes). A 50% overlap was used for the initial pass, and a 75% overlap was used for all subsequent passes. An gaussian window (elliptic in the streamwise direction) was applied to the correlation windows. The velocity fields were post-processed to remove spurious vectors, which were iteratively replaced if secondary correlation peaks were found, before the downstream and upstream images were combined. No interpolation, smoothing, or denoising was performed in post-processing.

Due to the nature of the plasma actuators used in these experiments (pulsed DC), electromagnetic interference (EMI) and radio-frequency interference (RFI) were significant concerns during data acquisition. Signal corruption could not only lead to excessively noisy data, but cause a mis-trigger event to occur between the laser, cameras, or microphones which would lead to garbage data. Great pains were therefore taken in order to isolate, shield and filter the electrical systems. A fiber-optic relay was designed and built in order to electrically isolate the plasma-generating equipment from the control computer (and ultimately the data acquisition systems). The plasma-generating equipment was also enclosed in a grounded metal rackmount cart to reduce the emitted RFI. Unfortunately, the building electrical grounds were also found to be corrupted by EMI, so additional filters were placed in stages along the trigger signal. A BenchMaster 21M Kemo filter, set to low-pass mode with a cutoff frequency of 99 kHz, was used to filter the flashlamp and q-switch trigger signals going into the laser power supply and head. Finally, between the LAFPA control computer and the PIV programmable timing unit input trigger a set of custom inductor-capacitor, resister-capacitor, and transient-voltage-suppressor filters were used.

## Chapter 3: The Pressure Signature of Aeroacoustic Sources

The genesis for this project first began with the work of Sinha *et al.* [? ], which studied the irrotational near-field response of a subsonic jet subjected to excitation with plasma actuators by decomposing the instantaneous fluctuating pressure field into a coherent ‘wave’ component (which corresponds to the large-scale structure generated by the excitation) and incoherent residual fluctuations (which correspond to the natural turbulence in the jet). Fundamentally, this decomposition is similar to the triple decomposition used by Hussein & Reynolds [? ]. Sinha *et al.* found that each pulse from the actuators produces a coherent large-scale structure that would grow, saturate, and decay as it advects through the jet shear layer.

In the irrotational near-field, the signature of these large-scale structures takes the form of a compact waveform. At low enough excitation frequencies, the characteristic period of this waveform is much less than the excitation period, and hence, the structures seeded by the excitation do not interact with one another as they evolve downstream. Therefore, their behavior can be thought of as representing the response of the jet to a single perturbation; in short this is the ‘impulse’ response of the jet, which is produced by the impulsive excitation by LAFFPs. As the period of actuation approaches the characteristic period of the impulse response, the waveforms extracted by the phase-averaging technique are largely unmodified from that of the

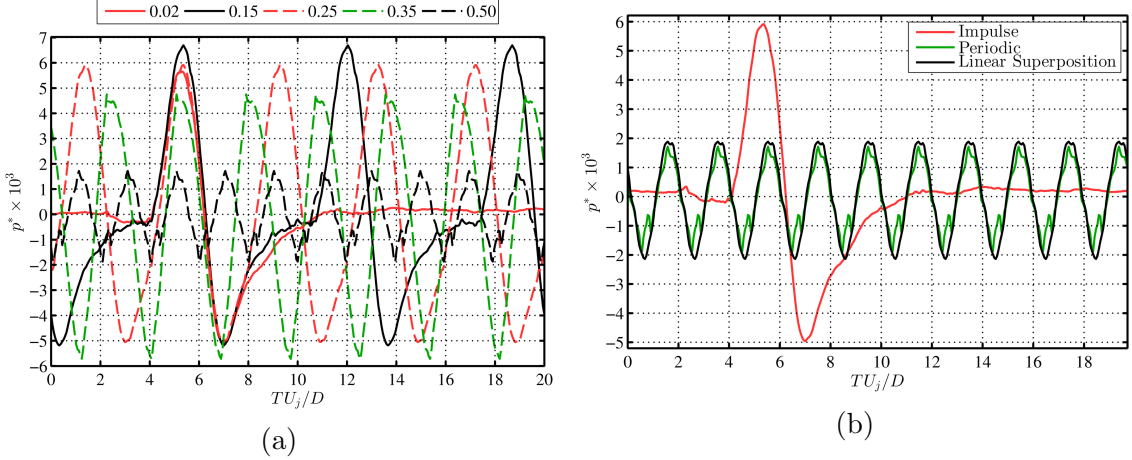


Figure 3.1: Phase-averaged waveforms along the first array position at  $z/D = 3, r/D = 1.35$  (a) and a linear superposition of the phase-averaged waveform for the impulse excitation ( $St_{DF} = 0.05$ ) compared against periodic excitation ( $St_{DF} = 0.50$ ) (b).

impulse response. Above this frequency, significant interaction between the structures is observed, with noticeable modifications to the waveform shape and amplitude. As the structures are growing as they advect through the shear layer, the frequency at which the structures begin to interact is dependent on the axial location. This behavior can be observed in Fig. 3.1a.

For a certain range of excitation frequencies ( $St_{DF} \leq 0.50$  at  $z/D = 2$ , for example), the structures interact in a quasi-linear manner, insofar as their near-field pressure signatures are concerned. To be precise, the response of the jet in the irrotational near-field could be well-predicted by a linear summation of the impulse response of the jet, repeated at the periodic excitation frequency. This concept has been illustrated in Fig. 3.1b, where the periodic response of the jet to excitation with  $St_{DF} = 0.50$  has been reproduced at  $z/D = 3.8$ . Additionally, a linear superposition of the impulse response for  $St_{DF} = 0.05$ , repeated to match the excitation frequency

of  $St_{DF} = 0.50$ , has been overlaid. The linear superposition has been arbitrarily shifted in time in order to match the phase of the periodic response; this phase difference is likely due to the dependence of convection velocities on structure frequency [? ] (or more accurately, structure size). For reference, the impulse response has also been included in the plots. Upstream of the end of the potential core ( $x/D \simeq 6$ , as will be found in §4), the quasi-linear interaction model produces close predictions of the waveform amplitude and shape, despite the significant difference in both peak amplitude and waveform shape between the impulse and periodic responses.

This quasi-linear interaction of the jet response to excitation is not limited exclusively to the hydrodynamically-dominated regions of the jet, but in fact holds for the acoustic far-field as well, at aft angles (where the acoustic signal is strongest and is known to correlate well with large-scale structures). This can be observed in Fig. 3.2a, where the phase-averaged response of the jet has been plotted for the far-field signal at a polar angle of  $30^\circ$ . For legibility, only a select number of excitation Strouhal numbers have been included. As with the irrotational near field, the acoustic far field exhibits a compact waveform for the lowest excitation Strouhal numbers. Though nearly a direct inverse from the waveform observed in the hydrodynamically-dominated near field, the far-field waveform is quite reminiscent of the phase-averaged waveforms observed by Kambe & Minota [? ] for the acoustic radiation towards aft angles produced by the head-on collision of vortex rings. At higher  $St_{DF}$ , a continuous oscillation between sharp expansion and compression waves is again observed, though the amplitude begins to decay above moderate excitation Strouhal numbers.

As before, a linear superposition of the impulse response can well predict the waveform shape and amplitude at the higher excitation frequencies (Fig. 3.2b), though in

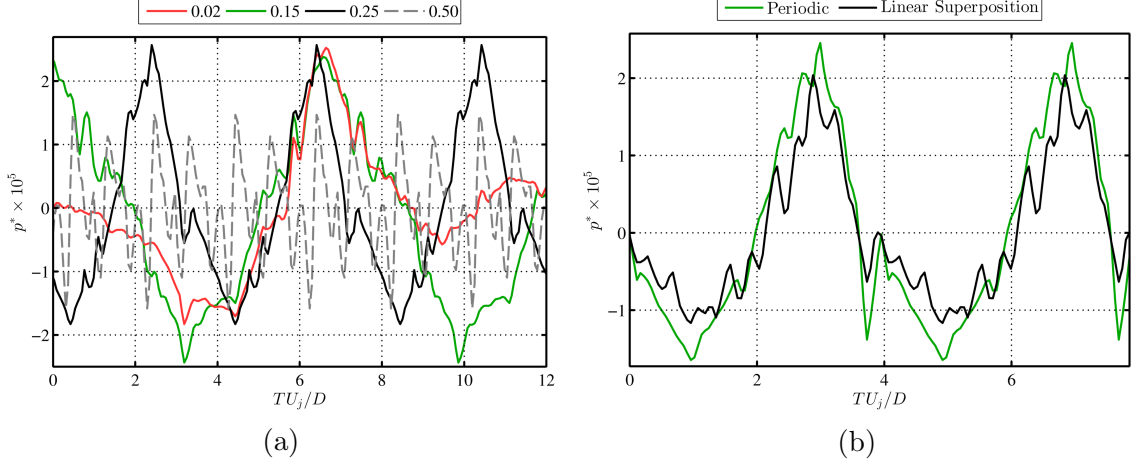


Figure 3.2: Phase-averaged waveforms of the far-field at  $30^\circ$  (a) and a linear superposition of the phase-averaged waveform for the impulse excitation ( $St_{DF} = 0.05$ ) compared against periodic excitation ( $St_{DF} = 0.25$ ) (b).

this case only up to  $St_{DF} = 0.25$ . From the phase-averaged waveforms alone it is not clear whether this breakdown in the linear superposition model at the highest excitation frequencies is due to nonlinear behavior or uncertainty in the phase-averaging. The phase-averaged waveforms were also investigated at polar angles of  $60^\circ$  and  $90^\circ$ ; however a clear waveform was not identifiable over the statistical uncertainty inherent in the phase-averaging process (likely due to the superdirective character of the acoustic radiation [?], which renders the amplitude at sideline angles too low to be detectable). Additional details and analysis of the phase-averaged near- and far-field signals can be found in Crawley *et al.* [?].

### 3.1 Preprocessing: Filtering the Actuator Self-Noise

Analysis of the near-field response of the forced jet is not immediately straightforward due to acoustic contamination from the actuators themselves [?]. LAFPAs

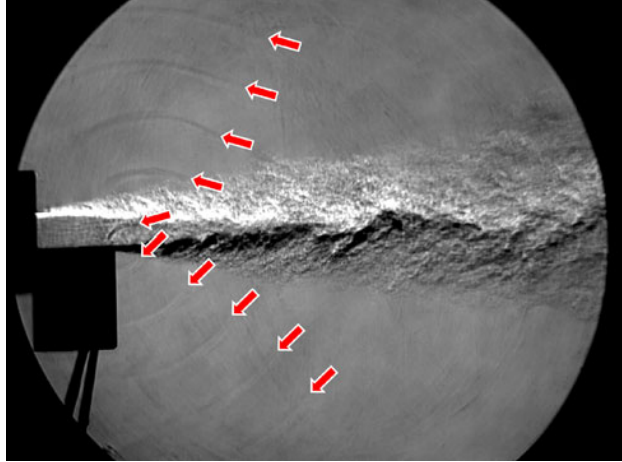


Figure 3.3: Schlieren image highlighting LAFPA compression waves. Reprinted from Samimy *et al.* [13].

operate on a joule heating principle: the breakdown of the air between the electrodes and the ensuing flow of current results in intense heating of the air. This rapid, localized thermal perturbation produces a compression wave, which excites the shear layer. However, this compression wave is still evident as it travels through the near field. Multiple compression waves can clearly be seen in Fig. 3.3, in which a subsonic rectangular jet is being excited at 20 kHz by four LAFPAs on its lower edge.

Obviously, this is an undesirable effect, as this actuator self-noise may in some cases obscure the hydrodynamic and acoustic response of the jet. So, in the present work the near-field pressure signals have been preprocessed using a continuous-wavelet-based filtering algorithm, which has been specifically designed to remove the actuator self-noise while leaving the signature of the jet response unaltered. An example of this filtering can be found in Fig. 3.4, where the raw and preprocessed signals have been plotted for  $St_{DF} = 0.02$  at  $x/D = 1$ ,  $r/D = 1.20$ . To aid in visualization, the results for multiple excitation periods has been phase-averaged to produce these waveforms.

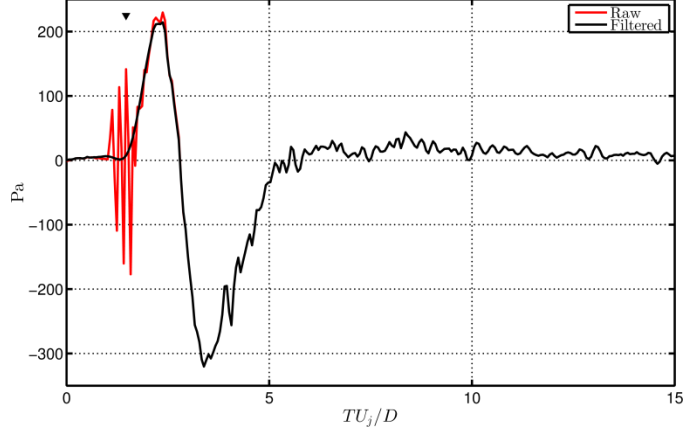


Figure 3.4: Raw and preprocessed near-field pressure.

As the actuator self-noise is localized in both time and frequency and can be well predicted, a smoothing algorithm in the wavelet domain was found to be the most effective method for removing the undesirable noise while leaving the response of the jet intact. A fourth-order Paul wavelet is employed, due to the similarity of its imaginary component to the phase-averaged response of the jet. As a result, the energy of the response of the jet is well defined in the wavelet domain, with the actuator self-noise existing as high-frequency, temporally-localized oscillations superimposed on the field. After smoothing in the wavelet domain to remove these oscillations, the signal is transformed back into the physical domain where it undergoes another smoothing operation in order to remove small amplitude, high frequency oscillations which may be introduced by the wavelet-smoothing. For consistency hereafter, all results examined within this work have been computed from the filtered, rather than the raw, signals.

### 3.2 Acoustic/Hydrodynamic Decomposition

Much of the difficulty in identifying the aeroacoustic source terms revolves around the dissimilar range of scales and fluctuation intensities of the turbulent eddies in the shear layer and the resulting radiated noise. Outside the jet shear layer, in the irrotational near-field of the jet, strong hydrodynamic pressure fluctuations associated directly with the passage of coherent structures in the shear layer and their resultant weak acoustic radiation coexist [Arndt]. Beyond this, in the acoustic far-field, the hydrodynamic signature of the coherent structures is nonexistent owing to their strong exponential decay with radial distance. It is in the irrotational near-field that much work has focused, in order to improve the aeroacoustic community's understanding of the link between shear layer turbulence and far-field acoustic radiation.

Owing to the presence of strong hydrodynamic fluctuations dominating the irrotational pressure field near the noise source regions, identification of pure acoustic waves and their corresponding source events is problematic. A decomposition of the pressure field into its constitutive hydrodynamic and acoustic components is therefore required. By identification and prediction of coherence nulls in the near field, Coiffet *et al.* [? ] showed that the full irrotational near-field consistent primarily as a linear superposition of its hydrodynamic and acoustic components, which lead subsequent researchers to propose linear filters to extract the individual components from the near-field pressure, with varying degrees of success.

As discussed by Tinney & Jordan [? ], in a transonic jet in which the large-scale structures are convecting subsonically with respect to the ambient speed of sound, a demarcation of the hydrodynamic and acoustic energy fields can be observed with phase velocity. This is because the hydrodynamic pressure fluctuations will be aligned

with the jet axis, and travelling subsonically. Acoustic pressure fluctuations will impinge on the linear microphone array at oblique angles, and therefore will appear as having either sonic or supersonic phase velocity, based on the source location. Therefore, a demarcation between the hydrodynamic and acoustic energy components should be readily identifiable about the sonic wavenumber,  $k_a = \omega/a_\infty$ .

An illustration of this can be found in Fig. 3.5, where the power spectral density of the irrotational near-field pressure for a single microphone array position has been plotted as a function of normalized frequency and (axial) wavenumber. The sonic velocity has been identified with a dashed line; energies lying above this line correspond to supersonically traveling waves (and hence, acoustic energy) whereas energies below this line correspond to subsonically convecting waves (hydrodynamic energy). Note that at high wavenumber and frequencies, two distinct energy lobes become readily apparent.

This phase-velocity separation is the basis for the decomposition method of Tinney & Jordan [?], which used a Fourier-based wavenumber-frequency filter in a cold, subsonic jet to separate the near-field pressure into supersonically- and subsonically-convecting waves. The pressure field is first transformed into Fourier space  $(k_x, \omega)$ , as

$$\hat{p}(k_x, \omega) = \iint_{\mathbb{R}^2} p(x, t) e^{-i(\omega t - k_x x)} dx dt \quad (3.1)$$

From the transformed pressure field, the hydrodynamic and acoustic fields can then be reconstructed separately, from

$$p_c(x, t) = \frac{1}{(2\pi)^2} \iint_{\mathbb{R}^2} \phi_c(k_x, \omega) \hat{p}(k_x, \omega) e^{i(\omega t - k_x x)} dk_x d\omega. \quad (3.2)$$

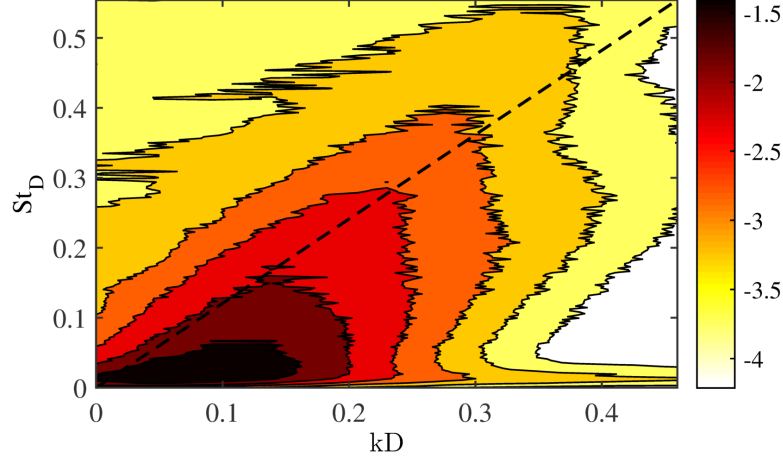


Figure 3.5: Wavenumber-Frequency spectral energy.

The component weight vector,  $\phi_c \in [0, 1]$ , is set based on the measured axial phase velocity,  $c = \omega/k_x$  in order to filter out either the supersonic or subsonic portion of the spectra.

Grizzi & Camussi [? ] took a slightly different approach, which utilized a discrete wavelet transform at individual spatial locations in order to decompose the fields based on an energy cutoff. The energy threshold was set iteratively, using analysis of two-point correlations of the acoustic and hydrodynamic components between two microphones, in order to ensure that realistic phase-velocities for the components were met. The Empirical Mode Decomposition (EMD) based method of Kuo *et al.* [? ] dispensed with explicit concerns with the phase velocity of the pressure components and instead used the critical frequency, as defined by Arndt *et al.* [46], which demarcates the energy dominance of the acoustic and hydrodynamic components in the near-field spectra.

In the current work, the irrotational near-field pressure is decomposed into its constitutive hydrodynamic and acoustic components based on phase-velocity. The current method is similar to that of Tinney & Jordan [? ] in that an axial array of many microphones is used, though it differs in how it identifies components of different phase-velocity. Here, the filtering will be performed by a spatio-temporal continuous wavelet transform.

### 3.2.1 The Wavelet Transform

Fourier analysis is commonly employed in the aeroacoustics community to study fundamental aspects of jet noise due to its simplicity and the great abundance of information it can provide. However, there is also a great drawback associated with Fourier analysis: while it analyzes a given signal at a distinct frequency, local information for a given event is spread over all spectral coefficients. This is due to the fact that the basis functions used by the Fourier transform oscillate indefinitely. For a completely stationary signal this is not an issue, however it has become increasingly clear that the jet noise phenomenon is not a stationary process. Transient events, such as intermittency or the spatial and temporal modulation of a wavepacket, have been shown to be important in the noise generation process.

Morlet [? ] introduced the wavelet transform in an effort to overcome some of the shortcomings of the Fourier transform. Unlike the Fourier transform, the wavelet transform involves a convolution of the signal with a set of basis functions which decay to zero at the bounds. As a direct result, translation of the basis function in space and/or time is now meaningful. The basis functions (often referred to as the analyzing or daughter wavelets) are all derived from a single function, the mother

wavelet, which must satisfy certain criteria [47]. Most notable of these criteria is that of admissibility, which in essence requires that the wavelet must be of finite energy. In practice, it is also helpful to choose a mother wavelet which is well-localized in both the spatio-temporal domain and the frequency domain. For a given mother wavelet,  $\psi(\vec{x})$ , the daughter wavelets can be constructed as

$$\psi_d(\vec{x}; s, \vec{\tau}, \theta) = s^{-n/2} \psi(s^{-1} r_{-\theta}(\vec{x} - \vec{\tau})) \quad (3.3)$$

where  $s$  is the scale factor,  $\vec{\tau}$  the translation parameter, and in the case of a multidimensional transform,  $r_{-\theta}$  is the rotation vector (which can be neglected for an isotropic mother wavelet). The  $s^{-n/2}$  factor ensures constant energy across all dilations. For a specific scale, translation, and rotation, the wavelet transform then becomes

$$\tilde{f}(s, \vec{\tau}, \theta) = \int_{\mathbb{R}^n} f(\vec{x}) \psi_d^*(\vec{x}; s, \vec{\tau}, \theta) d^n \vec{x}. \quad (3.4)$$

Because the basis functions of the wavelet transform are of finite energy, the locality of information in the original signal is preserved in the wavelet coefficients. This allows the identification, analysis, and reconstruction of localized events in the original signal, something not possible with the Fourier transform, which spreads temporal/spatial information over all transform coefficients. This has enabled previous researchers to perform a range of new analysis techniques to turbulence and acoustic phenomena not possible with the traditional Fourier transform. An excellent review of the development of wavelet analysis as well as applications to turbulence can be found in Farge [47].

Use of a multidimensional, continuous wavelet transform to extract intermittent events with a specific phase-velocity is not immediately straightforward, due to the

global nature of the scale factor. A ‘speed-tuning’ parameter,  $c$ , was introduced to the wavelet transform (now specifically referred to as a *spatio-temporal* wavelet transform) by Antoine *et al.* [?], who used it for use in motion tracking and identification in two-dimensional images. The definition for the daughter wavelets (3.3) is modified to

$$\psi_d(\vec{x}, t; s, \vec{x}', t') = s^{-n/2} \psi(s^{-1}c^{-1/n}(\vec{x} - \vec{x}'), s^{-1}c^{(n-1)/n}(t - t')) \quad (3.5)$$

where  $n$  corresponds to the total number of dimensions (temporal and spatial).

The continuous wavelet transform are isometry [? ] and hence is invertible. The original signal may therefore be recovered from the wavelet coefficients as

$$f(\vec{x}, t) = \frac{1}{C_\delta} \int_0^\infty \frac{ds}{s^{1+n/2}} \int_0^\infty \frac{dc}{c} \tilde{f}(\vec{x}, t, s, c). \quad (3.6)$$

The constant factor  $C_\delta$  serves as an energy scaling, and appears because we are reconstructing the signal using a different analyzing wavelet (in this case, a delta function) than the mother wavelet used in the forward transform [47? ? ]. For a given mother wavelet, this factor can be found from

$$C_\delta = \frac{1}{(2\pi)^n} \int_0^\infty \frac{ds}{s^{1+n/2}} \int_0^\infty \frac{dc}{c} \int_{\mathbb{R}^{n-1}} d\vec{k} \int_{-\infty}^\infty d\omega \hat{\psi}_d^* \quad (3.7)$$

where  $\hat{\psi}_d$  are the daughter wavelets in Fourier space. Since we are interested in decomposing the field into the acoustic and hydrodynamic components, a filtered reconstruction can be done quite easily in the wavelet domain by simply modifying the integration limits in Eqn. 3.6 to include only speed-tuning parameters corresponding to the subsonic or supersonic portion of the wavelet spectrum.

In this way, this methodology can be thought of as a simple modification of that proposed by Tinney & Jordan [? ], replacing the Fourier transform in their method with a spatio-temporal wavelet transform. The relationship between the wavelet

transform and the Fourier transform can be further elucidated by computing the forward transform in the Fourier domain (with the use of the convolution theorem), inserting this into Eqn. 3.6, and reversing the order of the integration:

$$f_c(\vec{x}, t) = \frac{1}{(2\pi)^n} \int_{\mathbb{R}^{n-1}} d\vec{k} \int_{-\infty}^{\infty} d\omega \hat{f}(\vec{k}, \omega) e^{i(\omega t - \vec{k} \cdot \vec{x})} \\ \times \frac{1}{C_\delta} \int_0^\infty \frac{ds}{s^{1+n/2}} \int_0^\infty \frac{dc}{c} \hat{\psi}_d^*(sc^{1/2}k, sc^{-1/2}\omega) \quad (3.8)$$

$$f_c(\vec{x}, t) = \frac{1}{(2\pi)^n} \int_{\mathbb{R}^{n-1}} d\vec{k} \int_{-\infty}^{\infty} d\omega \hat{f}(\vec{k}, \omega) e^{i(\omega t - \vec{k} \cdot \vec{x})} \phi_c(k, \omega) \quad (3.9)$$

The appearance of Eqn. 3.9 is identical to that of Eqn. 3.2; the difference lies in how filter  $\phi_c$  is defined, either explicitly in the Fourier domain in the case of the Fourier filtering or implicitly by the shape of the chosen mother wavelet in the wavelet transform. As numerous other researchers have discussed, this leads to an alternative interpretation of the wavelet transform, that of a series of bandpass filters, the passband envelope, centroid, and width being dictated by the scale, speed, and mother wavelet [47? ].

In fact, computing the convolutions is much faster in the Fourier domain than in the physical domain, so Eqn. 3.9 is the preferred method for computing the spatio-temporal wavelet filter. The decompositions were performed along each radial microphone array position individually, using the (1+1) dimensional (space-time) Morlet wavelet as the mother wavelet:

$$\psi(x, t) = e^{i(k_o x + \omega_0 t)} e^{-(x^2 + t^2)/2} \quad (3.10)$$

which the reader will recognize as simply a plane wave modulated by a Gaussian. Though simplicity was a factor in this decision, previous results analyzing phase-averaged waveforms in the far-field found acoustic emissions with a characteristic

waveform that share some resemblance to the Morlet wavelet [? ]. The base oscillation frequencies,  $(k_0, \omega_0)$  were set to  $(\pm 5, 5)$  (the dual sign for  $k_0$  being necessary to recover both forward and backward traveling waves), and  $\hat{\psi}(k, 0) = 0$  and  $\hat{\psi}(0, \omega) = 0$  so as to ensure that the mother wavelet met the admissibility criterion.

As the microphone array is irregularly spaced in the axial direction, the pressure field was interpolated onto a regular grid of spacing  $1D$  before computation of the discrete Fourier transform. In the current work, the local speed of sound was chosen as the phase-velocity demarcation, as opposed to the ambient speed of sound which had been used by previous researchers [? ]. In our case, the jet under study is subsonic and unheated, meaning that the local speed of sound ( 320 m/s) is still greater than the jet velocity ( 287 m/s) yet lower than the ambient speed of sound ( 346 m/s) and hence is a better choice for this particular application.

### 3.2.2 Validation

Though broad in its view, a simple evaluation of the decomposition algorithm can first be made by examination of the radial decay of the pressure fluctuation intensities, as has been done in Fig. 3.6 at an axial position near the end of the potential core. Theoretical analysis by Ribner [41] and Arndt *et al.* [46] showed that the intensity of the full hydrodynamic field (as opposed to the inertial field alone) decays as  $I \sim r^{-6}$ . In contrast, the acoustic field has been shown to be well-approximated by the linearized Euler equations, which exhibit  $I \sim r^{-2}$  decay rates (that is, the field is dominated by spherically propagating waves). Hence, the individually processed microphone array positions can serve as an initial validation step for the radial decay of the decomposed fields.

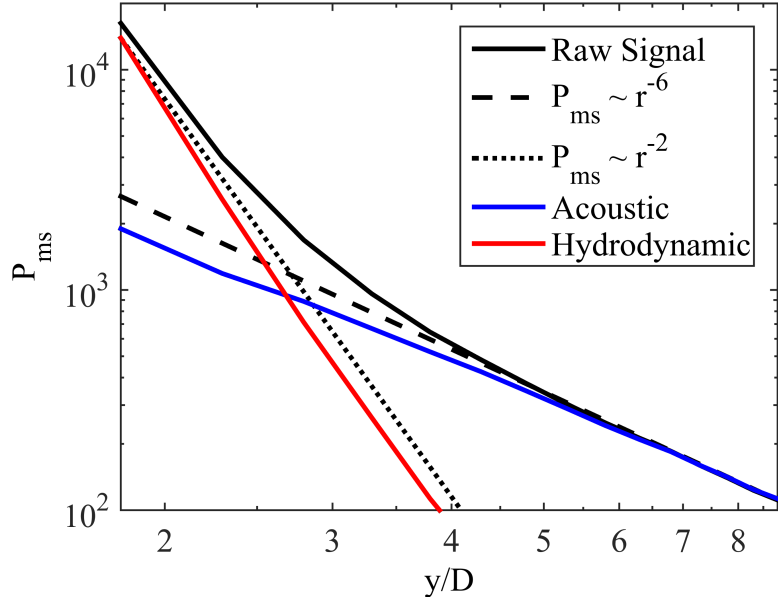


Figure 3.6: Radial decay of the raw signal compared against the theoretically-obtained and experimentally-measured decay rates for the acoustic and hydrodynamic components.

Comparison of the theoretical and measured radial decay rates for the decomposed acoustic and hydrodynamic fields can be found in Fig. 3.6. Overall, good agreement is found between the decomposed fields and the expected radial decay rates, indicating that on a broad level the decomposition algorithm is identifying and extracting the individual acoustic and hydrodynamic fields irrespective of the relative amplitudes of the two fields. However, it is observed that the decomposition produces an acoustic field which decays at a rate which is slightly slower than that dictated by spherically-spreading sound waves.

Further insight into the veracity of the recovered acoustic and hydrodynamic fields may be obtained through analysis of the energy spectrum. Like the radial decay rate of the pressure fluctuation intensities, Fourier analysis is inherently suited for random

processes and hence has been shown to miss certain important aspects of the jet noise process (e.g., intermittency). However, it has been used extensively throughout the aeroacoustic community for understanding the composition of both near-field pressure fluctuations as well as the acoustic far-field, to great success. Fundamental models in jet turbulence and aeroacoustics (e.g. the spectral decomposition of the irrotational near-field by Arndt *et al.* [46] and Tams similarity spectra for the acoustic far-field [1]) analyze their respective phenomena in the Fourier domain.

Sample spectra taken at  $z/D = 8, r/D = 2.2$  for the decomposed fields are shown in Fig. 3.7. In the case of the hydrodynamic field (Fig. 3.7a), the decomposed signal has been plotted against the raw near-field pressure spectrum as well as the  $I \sim k^{-6.67}$  spectral decay rate in log space (with frequency/wavenumber) that was identified by Arndt *et al.* [46] as the decay rate for the inertial subrange of the irrotational near-field. As one would expect for positions just outside the jet shear layer, the decomposition has identified the dominant spectral energy of the near-field as being hydrodynamic; the decomposed hydrodynamic field accounts for nearly the entire energy of the raw signal at low frequencies. Beginning at moderate frequencies ( $St_D \simeq 0.15$ ) a divergence between the raw irrotational near-field and the decomposed hydrodynamic field is observed, due to the increasing relative intensity of the acoustic field. At frequencies above this threshold, the decomposed hydrodynamic field exhibits a decay rate that matches quite well with the theoretical prediction, over several orders of magnitude.

The decomposed acoustic spectrum acquired at this same near-field position is compared against the far-field acoustic signal simultaneously acquired at a polar angle of  $30^\circ$  in Fig. 3.7b. The acoustic spectrum has been scaled in amplitude in order to

account for spherical propagation of the waves; calculating the propagation distances requires an assumption on the acoustic source region, which is not initially known with certainty. As will be discussed in more detail in §??, by measuring the time delay in two-point correlations between the near-field microphones and the far-field microphone at  $30^\circ$  the location of the dominant acoustic source region can be identified. In brief, the region just upstream of the end of the potential core ( $z/D = 4$ ) will be identified as the source region for the coherent large-scale structures in the jet; the current validation uses this location as the source region to scale the spectral amplitudes. The signal at  $z/D = 8, r/D = 2.2$  was chosen for this task as it lies roughly along a  $30^\circ$  path from this assumed source region. Additionally, the spectra were adjusted per ANSI S1.26 [? ] in order to account for atmospheric absorption of the (primarily high-frequency) acoustic waves due to propagation through a humid medium; the spectra shown here correspond to lossless propagation. Lastly, the spectral peaks have been denoted by triangular markers at the top of the figure.

It is found that the decomposed acoustic spectrum accurately reproduces the high-frequency portion of the far-field spectrum, which is unsurprising, given that the near-field spectra are dominated by acoustic fluctuations over this range of frequencies (though this does reinforce the accuracy of the amplitude-scaling used in the analysis). Overall, the acoustic spectra extracted by the wavelet filter mirrors the far-field spectra quite well in terms of both spectral shape and amplitude, producing a ‘peaky’ spectrum in contrast to the much more broadband raw irrotational near-field. The spectral peak occurs at nearly the same frequency as in the far-field, and is within 2 dB of the peak amplitude. The one major inaccuracy of the wavelet-based

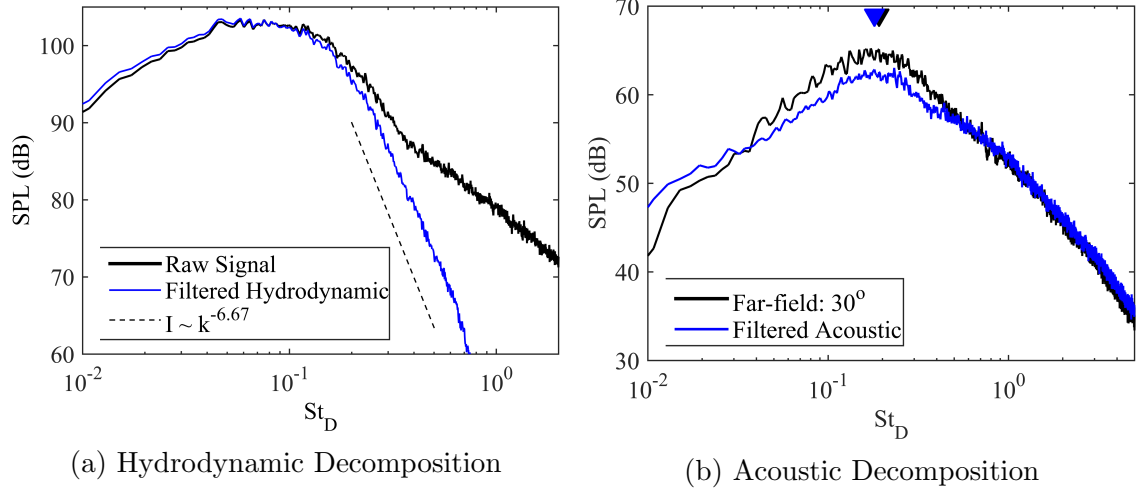


Figure 3.7: Spectral comparison of decomposed hydrodynamic field compared against the raw near-field signal (a) and decomposed acoustic field compared against the far-field acoustic signal at  $30^\circ$ . In both cases, the near-field signal was acquired at  $z/D = 8, r/D = 2.2$

method is the failure to accurately reproduce the low-frequency spectral decay rate of the far-field spectrum.

As a final method of validation, the decomposed fields for the excited jet were analyzed in the time domain by phase-averaging. As has been pointed out by numerous other researchers [7? ? ? ], the turbulent jet and resultant acoustic field are highly intermittent phenomena. An illustration of this behavior can be found in Fig. 3.8, where the wavelet power spectrum of the far-field at  $30^\circ$  has been plotted as a function of (pseudo) Strouhal number and time for the unforced jet; this can be compared against the Fourier power spectrum presented in Fig. 3.7b. As with the Fourier analysis, wavelet analysis demonstrates that the baseline jet radiates to the far-field over a broad range of Strouhal numbers, with the dominant energy occurring for  $St_{DF} \simeq 0.15$ . However, the far-field is found to be composed of temporally- and

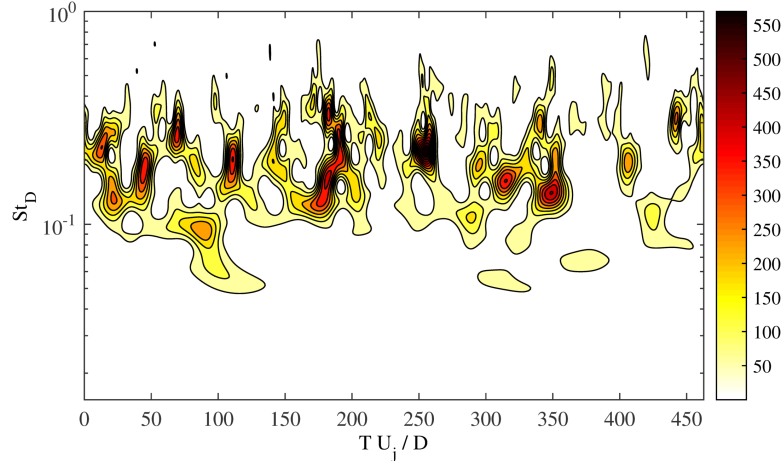


Figure 3.8: Wavelet power spectrum in the acoustic far-field at  $30^\circ$  for the natural jet.

frequency-localized bursts of energy far from the stationary field that Fourier analysis assumes. Clearly, this intermittent behavior needs to be recovered in the near-field by the decomposition process; something which may be evaluated with the aid of LAFPA excitation.

As before, the decomposed acoustic signal at  $z/D = 8, r/D = 2.2$  was propagated to the far-field at  $30^\circ$  by scaling the amplitude according to  $I \sim r^{-2}$ ; the phase-averaged signal was also shifted in time based on the ambient speed of sound in order to account for the propagation delay. Results of this procedure can be found in Fig. 3.9 for the jet excited at  $St_{DF} = 0.05$ . For illustrative purposes, results computed using the more standard Fourier-based decomposition method have also been included here. Both the Fourier and wavelet methods identify a distinct waveform which matches quite well with the waveform observed in the far-field, though with some discrepancies. The wavelet-method produces a slightly more accurate peak amplitude and event temporal extent. The most significant difference between Fourier and



Figure 3.9: Comparison of phase-averaged waveforms produced by excitation at  $St_{DF} = 0.05$ . As before, the near-field signal was acquired at  $z/D = 8, r/D = 2.2$

wavelet methods is the existence of severe ringing (caused by Gibbs phenomena) observed in the Fourier results just preceding the acoustic event. This phenomena persists even when the events are no longer strictly intermittent, (not shown here for brevity).

In the case of a subsonically-convection jet, the conceptual basis behind the Fourier decomposition algorithm is not in error (excluding the periodicity assumed by the Fourier transform). Instead, the practical requirements of discretely sampled microphones spanning a finite region in space, in addition to noise in the data acquisition, lead to numerical artifacts in the reconstructions. The Fourier transform required an extensive axial array of microphones (16 microphones spanning  $21D$  in the current study) in order to accurately represent the pressure fluctuations (the array was

originally designed with the intent of using the Fourier-based decomposition). This is because the basis functions (trigonometric function) used in the Fourier transform are not physically representative of the physical phenomena under study. As discussed previously, the turbulent jet (and resultant acoustic field) is highly intermittent. Even with the excitation producing regular large-scale structures, these, as well as the resultant acoustic emissions, exist as temporally and spatially localized energy bursts, rather than space-filling sinusoidal waves (as assumed by the Fourier transform). It has been shown that by using a temporally/spatially localized fluctuation as a basis, the wavelet transform compresses the information in a turbulent field much more efficiently (and accurately) than the Fourier transform [47].

Though there are some relatively minor discrepancies between the expected acoustic near-field and the one produced by the spatio-temporal wavelet filter, overall the results are promising. The decomposition algorithm is extracting hydrodynamic and acoustic fields which accurately reproduce the expected radial and frequency decay rates per theoretical analysis over the large domain investigated in this work (both in terms of spatial and frequency/wavenumber extent). Additionally, this accuracy is also not just a statistical phenomenon, as the decomposition algorithm is also found to accurately identify and reconstruct strongly-energetic, localized bursts of energy in the constitutive fields. Based on these results, the author felt confident that the decomposed acoustic field produced by the spatio-temporal wavelet filter was highly representative of the true acoustic near-field.

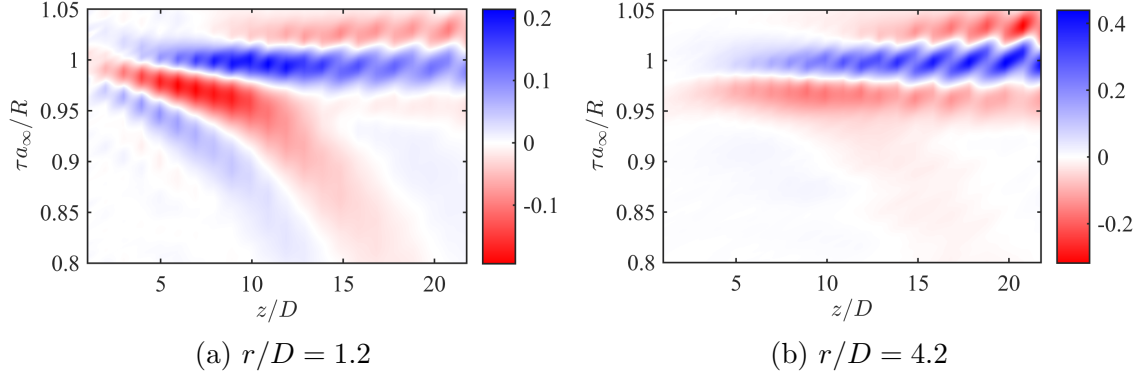


Figure 3.10: Normalized two-point correlations for the natural jet between the near field and the far field at  $30^\circ$  for two microphone array positions.

### 3.3 Identifying the Acoustic Source Region

Correlation analysis has long been used by researchers as a simple tool to quantify the relationship between two or more signals separated either by space or time. In its simplest form, two-point correlations measure the similarity and phase delay by a linear convolution of two signals. It is perhaps unsurprising then that two-point correlations are ubiquitous in fluid dynamics research. In this work, they will be used to better understand the relationship between the near-field dynamics and the acoustic radiation reaching the far field at aft angles. Correlations were computed (using the measured signals, as opposed to the phase-averaged waveforms) between each microphone in the near field and the far-field microphone at  $30^\circ$ . The correlations were then examined in the spatio-temporal domain, which showed distinct regions of positive and negative correlation spanning several jet diameters and flow time scales.

This behavior can be observed in Fig. 3.10, where the two-point correlations between the near-field and the far-field at  $30^\circ$  for two microphone array positions (starting at  $z/D = 1, r/D = 1.20$  and  $z/D = 1, r/D = 4.20$ ) have been plotted. The time lag,  $\tau$ , in the figures have been non-dimensionalized by the ambient speed of sound,  $a_\infty$ , and  $R$ , the distance from each near-field microphone to the far-field microphone (note that this results in an ordinate that is scaled separately along the abscissa, due to the dependence of the axial position on  $R$ ). Therefore,  $\tau a_\infty / R = 1$  corresponds to the time delay for an acoustic wave to travel directly from the near-field microphone to the far-field microphone.

Near the jet shear layer (Fig. 3.10a), four distinct correlation regions can be observed: two positive, two negative; one strong and one weak for each. The first correlation regions, the strong-negative and weak-positive, are noticeable beginning at the most upstream microphone and reach their peak values around  $5 < z/D < 10$ , decaying significantly beyond that. The slopes of these regions indicate propagation velocities noticeably below the sonic velocity; in the upstream region, they roughly match with the measured convective velocity of the large-scale structures ( $U_c \simeq 0.7U_j$  as measured by two-point correlations between subsequent near-field microphones, see Crawley *et al.* [? ] for additional details) in the upstream region of the jet, and slowly decelerate downstream. Similar behavior was observed by Bogey & Bailley [36], who noted that two-point correlations between the flow-field and acoustic near-field in a simulated jet produced strong positive correlation regions which peaked at the end of the potential core and which followed the convection of the large-scale structures. Conversely, the strong-positive and weak-negative correlation regions exhibit propagation velocities that match well with the ambient speed of sound. These correlation

regions start from almost negligible values upstream, strongly amplify near and just beyond the end of the potential core, and decay gradually in the most downstream region.

As the microphone array is moved radially outwards (Fig. 3.10b), the strong-negative and weak-positive correlation regions quickly decay to negligible values and all observable correlation regions begin to match the expected time-of-arrival for sonically-traveling waves. The distinctly different propagation velocities and axial and radial evolutions of the two pairs of correlation regions indicate that these correspond to different physical phenomena. The strong-negative and weak-positive correlation regions observed near the jet shear layer are associated with the large-scale structures themselves, rather than acoustic phenomena. The positive and negative correlation regions are likely associated with the braid and core regions of the large-scale structure as they convect through the shear layer. The low-pressure core region of the vortex produces a positive correlation value with the far-field acoustic due to the phase inversion of the acoustic waveform at low polar angles (Fig. 3.1). At this radial location, the dominant energy measured by the microphone array is acoustic, owing to the strong decay of the hydrodynamic field with radial distance from the jet [46]. Though they have not been included here for brevity, the two-point correlations in the excited jet cases show similar behavior, albeit with enhanced correlation levels particularly for the large-scale structure related regions.

This relationship becomes even more clear when just the acoustic component of the near-field is considered during computation of the two-point correlations, rather than the full irrotational near-field. Gone entirely now are the correlation regions with subsonic propagation velocities, even at the closest microphone array positions, as

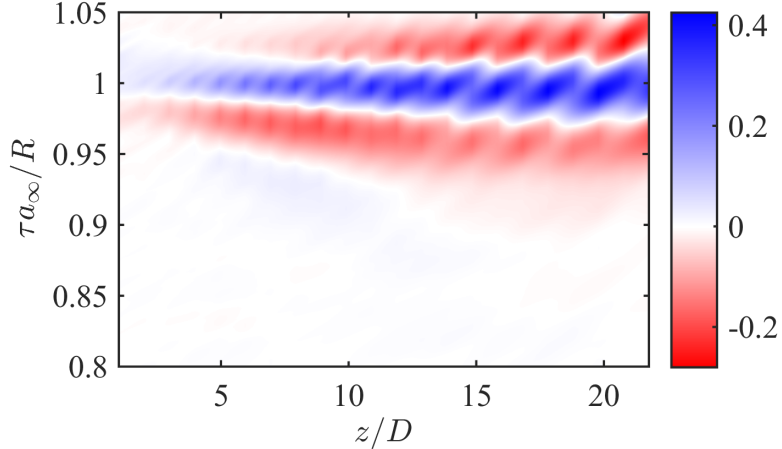


Figure 3.11: Normalized two-point correlations for the natural jet between the acoustic component of the near field and the far field at  $30^\circ$  for microphone array position starting at  $z/D = 1, r/D = 1.2$ .

can be seen in Fig. 3.11. Instead, a single positive correlation region corresponding to sonically-propagating waves exists over the entire domain with significantly enhanced correlation over the full field results. In fact, the results found here for the acoustic component along the first microphone array position are nearly identical to those for the full field response at the further away array positions (Fig. 3.10b), which were dominated by acoustic, rather than hydrodynamic, energy.

We can now use the correlations of the decomposed near-field in order to identify the acoustic source region, at least in a rough sense, by comparing the time lag at which the greatest correlation is achieved against expected times-of-arrival for different propagation paths. A schematic of these propagation paths is provided in Fig. 3.12. The first expected time of arrival,  $\tau_a$ , corresponds to the expected time lag for an acoustic wave traveling directly from the noise source to the near-field microphone and on to the far-field microphone and hence, the noise source region lies

along the axis created by the near-field and far-field microphones. Another expected time-of-arrival can be constructed by assuming the source region is stationary in space; from simple geometric considerations of the distance from the assumed source region to the near-field and far-field microphones, the time lag,  $\tau_s$ , between the arrival of an acoustic wave at both microphones can be computed. The stationary source region is of course not known *a priori*, but is set by the author subsequent to the computation of the two-point correlations.

For simplicity, density and convection effects on the acoustic wave as it travels through the jet shear layer have been neglected in this analysis. By necessity, it has been assumed that the acoustic radiation in the jet is dominated by  $m = 0$  azimuthal Fourier mode (the near-field and far-field microphone arrays are not at the same azimuthal angle with respect to the nozzle). This assumption is easily justified in the excited jets, where the actuators have been fired in phase. While the near-field pressure and acoustic radiation towards aft polar angles in a natural, high Reynolds number jet is a combination of numerous azimuthal Fourier modes, previous researchers have found these fields to be dominated by the axisymmetric mode [46? ? ?].

Here, the acoustic source region was assumed to be located at  $x_s/D = 4$ , which is just upstream of the end of the potential core in the unforced jet. (Please note that this analysis is not meant to imply that the source region is located at a specific, fixed point – it is merely a convenient way of understanding the propagation paths.) Similar behavior is observed between the natural jet and the excited cases in Fig. 3.13; note that due to numerical discrepancies at the domain boundaries (see Torrence & Campo [?] for a discussion of the ‘cone of influence’ of wavelet coefficients and the

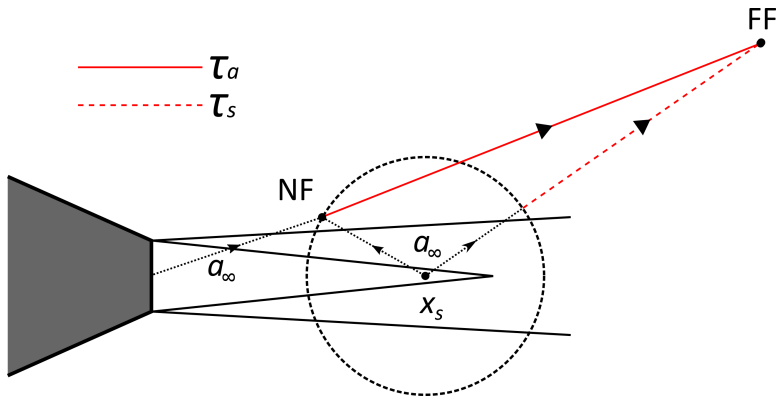


Figure 3.12: Expected times of arrival for on-axis acoustic propagation,  $\tau_a$ , and off-axis acoustic propagation,  $\tau_s$  from a stationary source region centered at  $x_s$ .

effect thereof), the correlation values have been truncated at the most upstream and downstream microphones. For the impulsively-excited jet, nearly identical correlation regions are observed between the excited and natural jet; in the periodically-excited jet continuous oscillations occur throughout time due to the similarity of continuously-generated large-scale structures and resultant acoustic radiation. In the upstream region of the jet, the peaks of the positive correlation region match  $\tau_a$  nearly exactly. In the downstream region,  $\tau_a$  begins to increasingly over-predict the time lag for the maximum correlation. On the other hand,  $\tau_s$  tracks the time lags for the peak correlation consistently over the downstream region, but not the upstream region. The results found here appear to indicate that the dominant acoustic radiation reaching the far-field aft angles is being generated over an extended region of the jet mixing layer, roughly  $z/D \leq 4$ , which is just upstream of the time-averaged end of the potential core in the natural jet. This is not too dissimilar from the findings of other researchers, who have suggested that the acoustic source region lies just *downstream* of the end of the potential core [? ]. That this source region is consistent between

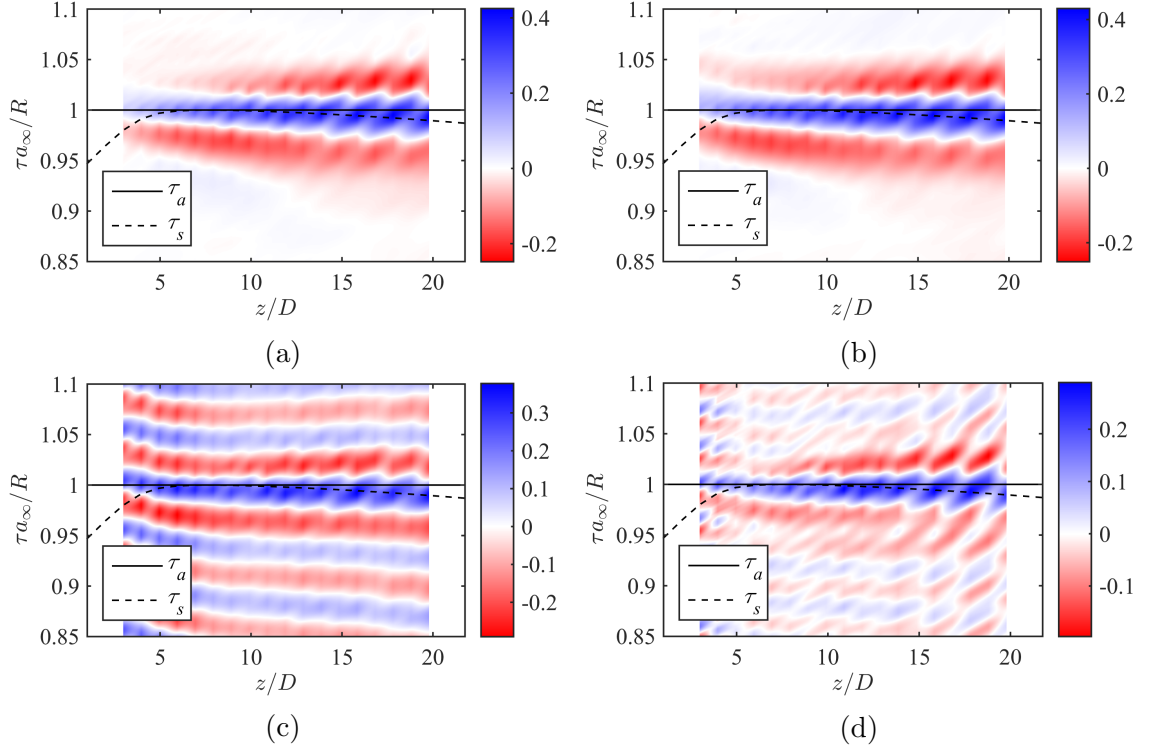


Figure 3.13: Normalized two-point correlations between the acoustic component of the near field and the far field at  $30^\circ$  for microphone array position starting at  $z/D = 1, r/D = 1.2$  for the natural jet (a),  $St_{DF} = 0.05$  (b),  $St_{DF} = 0.25$  (c) and  $St_{DF} = 0.35$  (d).

the excitation frequencies explored here is suggestive of a consistent dominant source mechanism, akin to the results presented in Fig. 3.2b.

The author would like to make a special note here, concerning the discrepancy between the results presented in Fig. 3.13 and those presented previously in Crawley *et al.* [? ]. In that paper, the more simple Fourier filter was used to decompose the irrotational near-field; processing artifacts were noted and a parametric study was attempted to minimize their impact. In the resulting two-point correlations of the decomposed acoustic field, a shift in the apparent source region was noted to coincide

with the shift of the peak pressure fluctuations measured just outside the shear layer (higher frequency excitation cases saturating further upstream near the nozzle exit). Because this behavior was observed across the entire range of filter parameters used, it was assumed to be representative of the true physical behavior and not a numerical artifact. Of course, this assumption precludes the possibility that *the entire parameter space produced similar numerical artifacts.*

As discussed more thoroughly Crawley & Samimy [cite], the Fourier filter had a tendency to allow energy leakage from the hydrodynamic field into the acoustic, particularly at low frequencies. Since it has already been observed that the hydrodynamic signature of the large-scale structures can linearly correlate to the acoustic emission, a potential consequence of this leakage is correlation regions which instead point to the region of high hydrodynamic energy - i.e. the saturation point of the near-field pressure fluctuations. There are few certainties in life beyond death and taxes, so it is difficult to argue with definitiveness that the results depicted in the present work are entirely free of numerical artifacts. However, the analysis found in Crawley & Samimy [cite] demonstrate that wavelet filter is more robust in this regard, and as such the author is inclined to lend more credence to the results presented herein. [Reference to results in chapter 5?]

## Chapter 4: Estimation of Time-resolved Velocity Fields

Analysis of the evolution and interaction of the large-scale structures, and ultimately the noise generated thereby, is greatly simplified by the acquisition of time-resolved flow-field measurements. (In fact, as will be discussed in §5, computation of the aeroacoustic source field will eventually require a temporal derivative and thus time-resolved data is a necessity for the current work.) Unfortunately, directly acquiring time-resolved velocity fields for the jet currently under study is simply not possible due to the combination of a large domain of interest ( $0 \leq z/D \lesssim 12, 0 \leq r/D \lesssim 3$ ) and high characteristic frequencies on the order of several kilohertz. Full-field, high-fidelity measurement techniques capable of this repetition rate simply do not exist at present. An indirect method is therefore required in order to estimate the evolution of the large-scale structures, in a reduced-order sense.

Phase-locking of a data acquisition system to actuators (or a naturally occurring resonance tone) is a common experimental technique; by varying the delay between the trigger and time of data acquisition, multiple phases can be acquired and the coherent component of the phenomena can be analyzed. Phase-locking of the PIV system to the LAFPAs was initially considered for the present work, but quickly discarded. Sample analysis performed using a numerical database indicated that a very high temporal resolution was required in order to accurately compute fluctuation

rates in the dilatation field (the relevance of which will become more apparent in the following chapter). At moderate to high excitation frequencies, this was feasible, though potentially tedious (for example,  $\sim 16$  phases were estimated as necessary at  $St_{DF} = 0.25$ ). At  $St_{DF} = 0.05$  however, this would require roughly *forty* phases (the significant dead time between actuations means that it is not necessary to acquire the entire range of phases from 0 to  $2\pi$ , but this is small consolation). Clearly, a more efficient data acquisition method is in order.

## 4.1 Stochastic Estimation

Stochastic estimation was first proposed by Adrian [? ] in 1977, as an outgrowth from the conditional statistical analyses popular at the time. Large-scale coherent structures had been educed from anisotropic turbulent flows (such as boundary or shear layers) by conditional sampling techniques. Adrian succeeded in identifying detailed flow structures ('conditional eddies') in isotropic turbulence by computing a mean-square estimate of the flow from linear two-point correlations (higher-order, nonlinear correlations were explored in Adrian [? ]). The methodology was extended in Adrian [? ] to estimation of velocity fields using spatial correlations coupled with a reduced set of measurements.

Stochastic estimation attracted considerable attention from the fluid dynamics community due to its potential to educe meaningful structures and behavior from highly turbulent, incoherent flows as well as its relative simplicity. Subsequent researchers refined stochastic estimation in several important aspects. Bonnet *et al.* [? ] developed the complementary technique by combining linear stochastic estimation (LSE) with proper orthogonal decomposition (POD), improving the accuracy

due to higher correlation levels between low-order modes. The estimated velocity fields produced by LSE were projected onto the POD eigenfunctions (computed from the random, non-time-resolved velocity fields) to produce an estimate of the time-dependent POD coefficients, which can then be used to reconstruct low-order representations of the estimated random velocity field. Picard & Delville [Picard2000] used LSE and POD to link the longitudinal pressure distribution surrounding a low subsonic jet to vortical motions in the shear layer by simultaneously sampling microphone and hotwire data. In Boree [? ] the POD coefficients of the velocity field were estimated directly, using pressure modes. Ewing & Citriniti [? ] extended the standard form of LSE, in which spatial correlations are computed at a single time lag, by Fourier transforming the reference signal in time prior to computing the two-point cross-correlations (now cross-spectra). The incorporation of phase-delay information over a range of frequencies (and in essence, including information from multiple time lags) was found to significantly improve the accuracy of the reconstructions for many flow regimes [? ] [Tinney2006,Tinney2008]. Finally, multi-time-delay LSE-POD was performed in the physical domain (as opposed to the Fourier) by Durgesh & Naughton [? ] to study the turbulent structures in a near wake region.

The current work borrows heavily from the methodology of Tinney *et al.* [TinneyJFM2008] and Sinha *et al.* [SinhaIJFC2010] in order to estimate the two-component time-resolved velocity field on a streamwise slice of the jet. As explained in §2.3.2, two-component PIV snapshots were acquired at well-defined instants of near-field pressure traces. The computational methodology by which the stochastic estimation is performed has been modified, however. Complementary stochastic estimation is used, due to its significantly lower computational cost as well as theorized improvement in

accuracy. Thus, the instantaneous velocity fields will be separated into characteristic modes via POD and the time-dependent modal coefficients, rather than the velocity fields themselves, will be estimated using SE. Instead of performing the stochastic estimation using either linear or higher-order cross-correlations (or cross-spectra), the conditional mapping between the near-field pressure and the POD modal coefficients will be generated by an artificial neural network with multi-time-delay. Artificial neural networks were chosen over the more traditional cross-correlations due to their simplicity compared to high-order methods as well as their demonstrated ability to model nonlinear processes in turbulent flows [Lasagna2015].

#### 4.1.1 Stochastic Estimation via Artificial Neural Networks

Artificial neural networks (ANNs), are statistical computing models which developed as a branch of machine learning. The design of neural networks is based on simplified models of the human brain: they are comprised of a large number of simple, interconnected computing cells ('neurons') and therefore are massively parallel distributed processors. The neurons themselves are based on models of biological neurons, and produce a single output based on the linear summations of inputs (either directly from the user or from other, lower-level neurons) and synaptic weights which is then modulated by a nonlinear activation function. The synaptic weights are modified by a learning algorithm in order to minimize a cost function; this generally takes the form of explicit training (supervised learning). The interconnectivity of a massive number of these nonlinear computing cells allows artificial neural networks to approximate unknown, nonlinear functions of an arbitrary number of inputs while retaining a certain, elegant, simplicity. It should be unsurprising then, that ANNs

have already been applied for the estimation and control of a variety of turbulent flow regimes. Interested readers are recommended to refer to Haykin [1994] for an extensive background on artificial neural networks, their developmental history, and many additional network structures not used in this work.

A feedforward network structure was used in the current work, a schematic of which can be found in Fig. 4.1. The ANN was comprised of an input layer, to which near-field pressure traces were supplied, a single hidden layer, and an output layer which produced estimates of the time-varying POD coefficients. The hidden and output layers were fully connected, and the modified logistic function (hyperbolic tangent) was used as the activation function. The pressure traces were centered around the acquisition of a PIV image group, and was downsampled to 100 kHz in order to match the frequency response of the microphones. The record time supplied for each training block was  $\pm 5.12$  microsecond; this was determined by estimating the time delay for a large-scale structure to convect through the experimental domain (the convective velocity of the large-scale structures was conservatively estimated as  $U_c \simeq 0.5U_j$ ).

POD modes and time-varying coefficients were computed from the velocity fields using the method of snapshots [Sirovich1987]; the kernel was defined as the two-component turbulent kinetic energy. The instantaneous velocity fields were not pre-processed prior to the decomposition (that is, missing or spurious vectors were not replaced or interpolated). As experimental noise in the velocity fields will be completely uncorrelated to the near-field measurements, it will be filtered out by the stochastic estimation and hence preprocessing is unnecessary. Unlike many past researchers, the coefficients for every POD mode were estimated, rather than just the

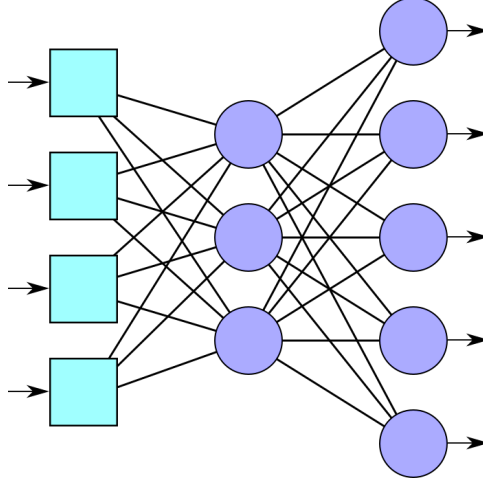


Figure 4.1: Schematic of a feedforward ANN with a single hidden layer. The activation function is applied only to the hidden and output layers. The number of neurons depicted in each layer is meant to represent the *relative* number used by the actual ANN.

most energetic modes, for two reasons. First, it is not guaranteed that an individual POD mode corresponds to a physically distinct turbulent flow structure or event - an event may be broken up into multiple POD modes of varying energy levels. Secondly, the most energetic POD mode(s) is not necessarily the most relevant mode(s) for the acoustic generation process (see Jordan *et al.* [2007] for a modification to the standard POD kernel in order to mitigate this issue).

Even though the network is estimating even the least-energetic modes, the current method is far more computationally efficient than directly estimating the velocity fields themselves. By encoding spatial correlations in the POD expansion coefficients, estimation of the  $N$  snapshots of  $M \times K$  spatial locations has been reduced from a minimization problem of  $N$  vectors of  $2MK$  to one of  $N$  vectors of  $N$ . For the current experimental database, this means the system has been reduced from  $290,508 \times$

1500 to  $1500 \times 1500$ . The neural network now only needs to identify the temporal correlations between the pressure field and the individual POD coefficients; it does not need to learn the spatial correlations.

Learning was accomplished via the standard backpropagation method [Haykin1994], which approximates the error surface of the cost function using first-order derivatives; the error ‘propagates’ backwards from the output neurons to the hidden neurons and the synaptic weights at each neuron are updated to identify the (hopefully, global) minimum of the cost function using gradient descent. The cost function was defined as the mean-squared-error between the predicted and measured expansion coefficients for a given PIV image group. The velocity field,  $\mathbf{U}$  at a given instance,  $k$ , can be recovered from  $N$  orthonormal modes,  $\phi$ , and time-varying expansion coefficients,  $a_k$ , as  $\mathbf{U} = \sum_{n=0}^N a_k^n \phi^n$  [Tinney2008]. The total energy of each mode is therefore encoded in  $a_k^n$ , which will serve as a simple energy weighting for the cost function (the importance of relative errors to the cost function will essentially be scaled by the energy in each particular mode). Training of the network was performed using the roughly 1500 ensemble pressure-velocity blocks of data (a few PIV images in each set had to be discarded due to laser misfires); synaptic weights were updated base on the average of all blocks (batch processing) using a constant learning rate. A well-known issue with the gradient descent optimization method is that it has a tendency to get trapped in local minima and fails to converge to the global minimum. Therefore, sample results were also calculated using a much different learning algorithm: adaptive particle swarm optimization. Details will not be presented here however, as the results were found to not differ substantially from those produced by the backpropagation algorithm (while requiring significantly higher computational resources).

### 4.1.2 Reduced-Order Representation of the Flow-Field

Ultimately, due to limitations both in the methodology as well as in the ability of the microphones to sense fine-scale turbulent fluctuations, the estimated velocity field is going to represent a reduced-order model of the jet. This can be easily observed in Fig. 4.2, where the measured axial velocity field at an arbitrary instance in time has been plotted against the velocity field produced by the SE-POD estimation from the near-field pressure at the same instance in time. For comparison purposes, a reduced-order reconstruction of the measured velocity field from the first 100 POD modes (but without estimating from the near-field pressure using SE) has also been included. Note that here the output of the model produced by SE-POD is being compared against a known output that the system is meant to match; this is not an evaluation of the *predictive* power of the model but of the *representative* power.

As one would hope, the large-scale turbulent fluctuations are correctly identified by the SE-POD algorithm, and a mapping from the near-field pressure to this structures is appropriately generated. The accuracy in the feature reproduction degrades considerably however as the scale of the turbulent eddy is reduced. Some small-scale behavior is retained though most is filtered out, particularly the downstream region. This was entirely expected however, as the reference signal is much more strongly damped with wavenumber than the conditional field being estimated (decay rates of  $-20/3$  for the pressure field versus  $-5/3$  for the velocity field). The pressure field simply does not have the resolution to approximate the velocity field, particularly further downstream where the microphones are further from the jet centerline due to the spreading of the shear layer. The estimated velocity fields are specifically referred to in the present work as *reduced*-order rather than *low*-order however. Comparison

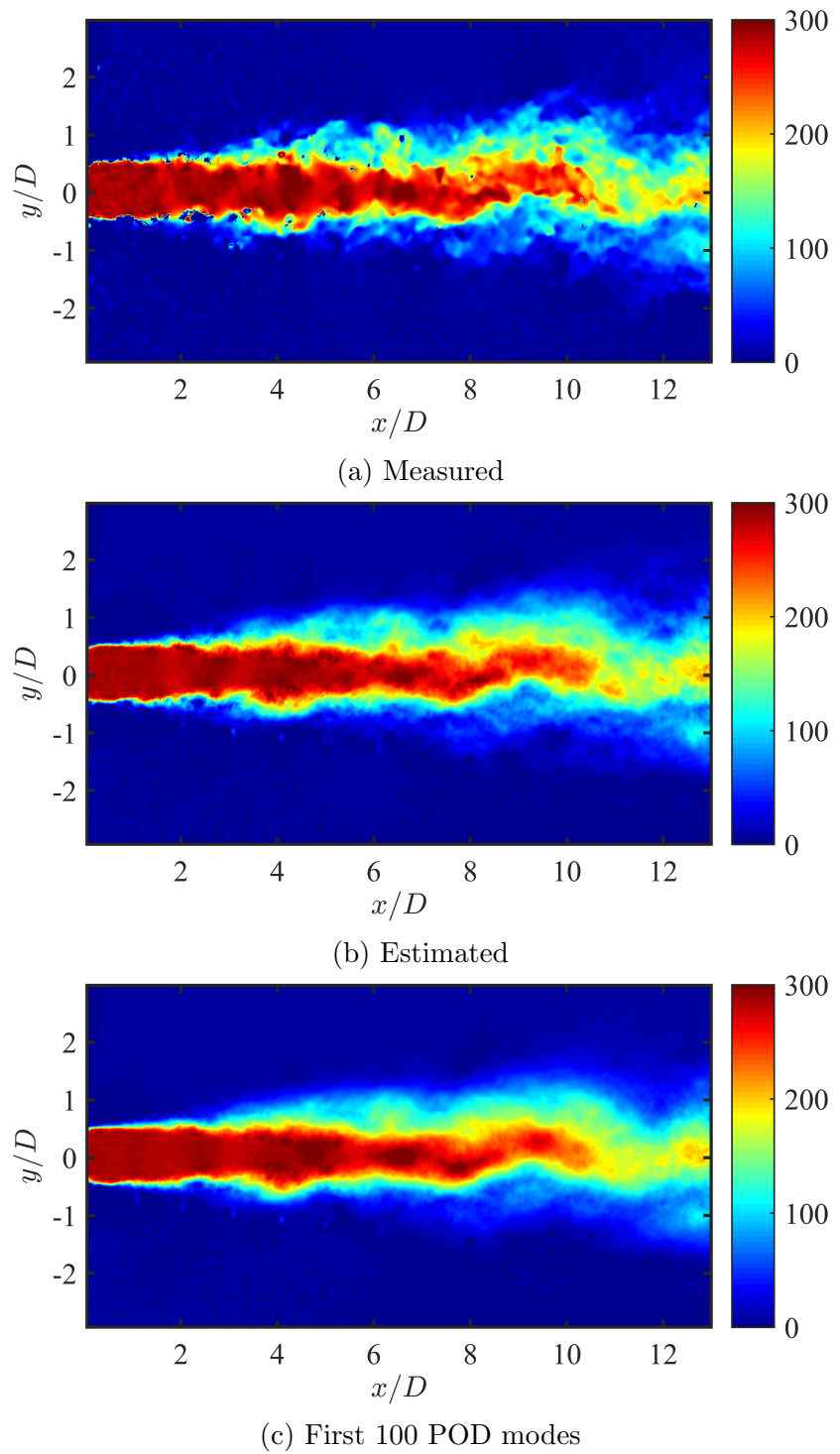


Figure 4.2: Comparison of a raw instantaneous axial velocity field  $St_{DF} = 0.05$  (a) against the same velocity field estimated from the near-field pressure (b) and finally a reduced-order reconstruction of the raw velocity using the first 100 POD modes ; units are in m/s.

of the estimated velocity against a reconstruction of the measured field using the most energetic 100 POD modes (of a total of 1500 POD modes corresponding to the 1500 uncorrelated velocity fields) indicates that the SE-POD algorithm is retain similar (if not greater) energy levels. An example of this is the small-scale structure observed at  $x/D \simeq 8$ , just outside the high-velocity region of the jet (orange, in the figure in the measured velocity. This distinct structure is still visible (though smeared and slightly reduced in amplitude) in the estimated velocity, though it is basically nonexistent in the 100-mode reconstruction which contains  $\sim 50\%$  of the fluctuating energy (see Fig. 4.5). While it is unlikely that this particular structure is notably important to the acoustic emission of the jet, low modal energy modulations of the large-scale structures may be. Hence, it is desirable to retain as much of the information as possible when estimating the flow.

As a side note, the measured velocity fields retain some experimental errors from the PIV data processing; for instance, the small pockets of zero axial velocity observed on lower shear layer (particularly for  $2 < x/D < 4$ ) in Fig. 4.2 are non-physical and correspond to missing vectors. As these experimental errors will be completely uncorrelated from the pressure signals, a conditional reconstruction will have great difficulty in reproducing them; in fact they *should not* map from the pressure to the velocity at all.

It is also important to be mindful that an individual POD mode may not in fact correspond to anything physically distinct in the turbulent flow - it is after all, merely a mathematical construct which is based on no *a priori* information of the system under investigation. Tinney *et al.* [Tinney2008b] noticed that the modes produced by (spectral) POD had a tendency to appear in coupled pairs, and similar behavior

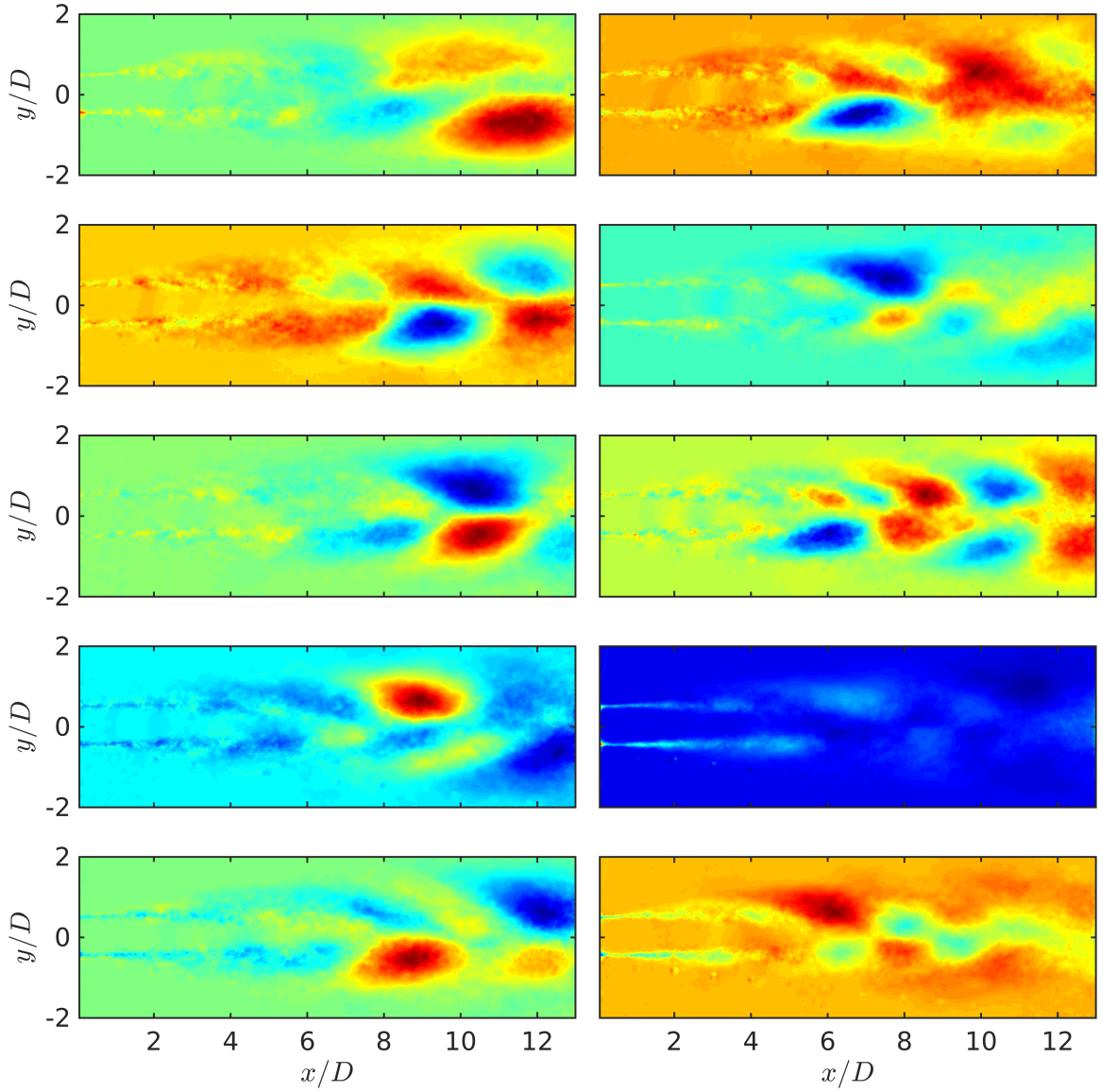


Figure 4.3: First 10 POD modes for  $St_{DF} = 0.05$ , ordered top-down and then left-right.

is observed here. For reference, the ten most energetic POD modes are shown in Fig. 4.3 for  $St_{DF} = 0.05$  and Fig. 4.4 for  $St_{DF} = 0.25$ .

1. Comparison of estimated, phase-averaged estimated, and phase-averaged at  $\phi = 0, \pi$

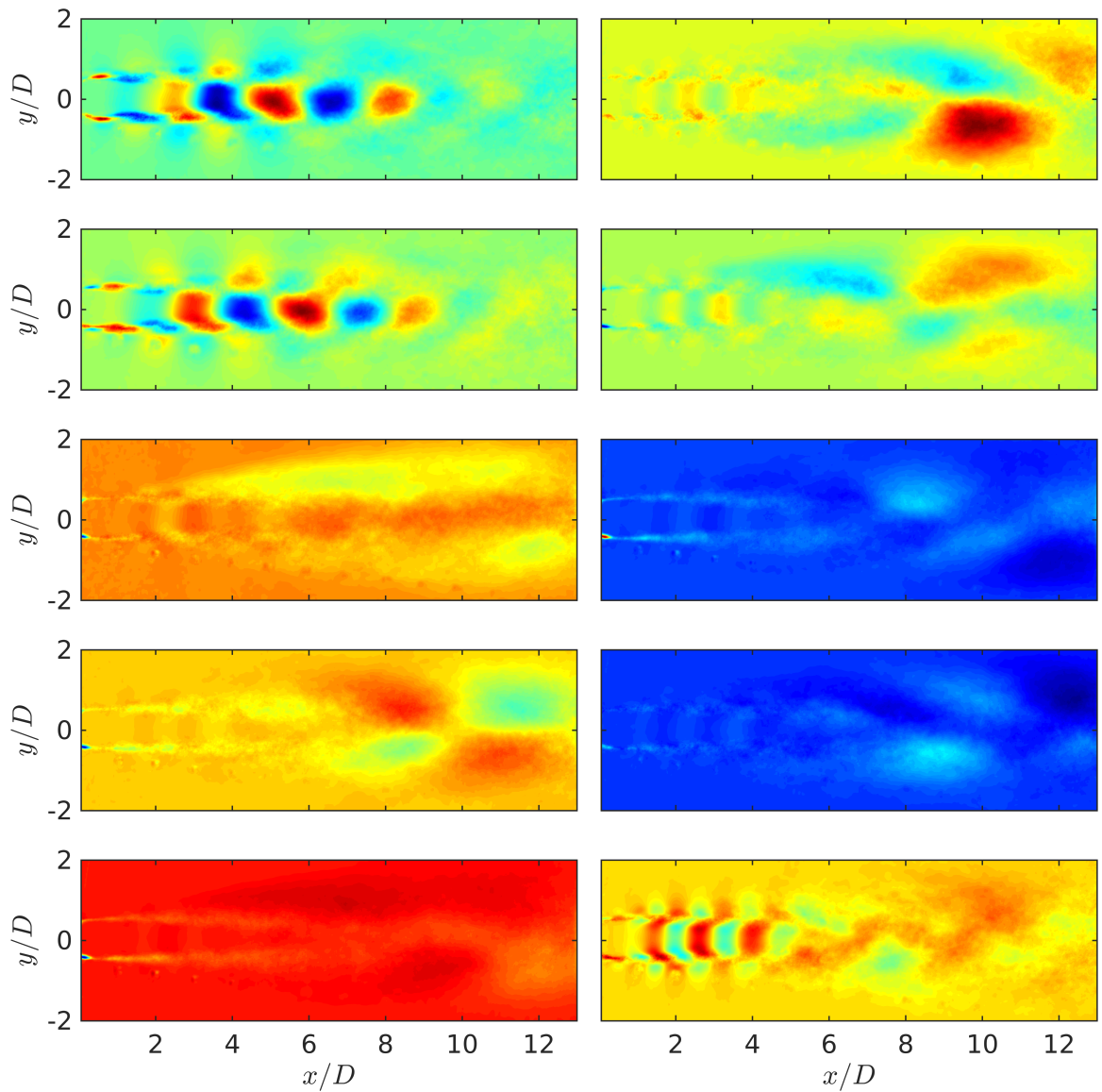


Figure 4.4: First 10 POD modes for  $St_{DF} = 0.25$ , ordered top-down and then left-right.

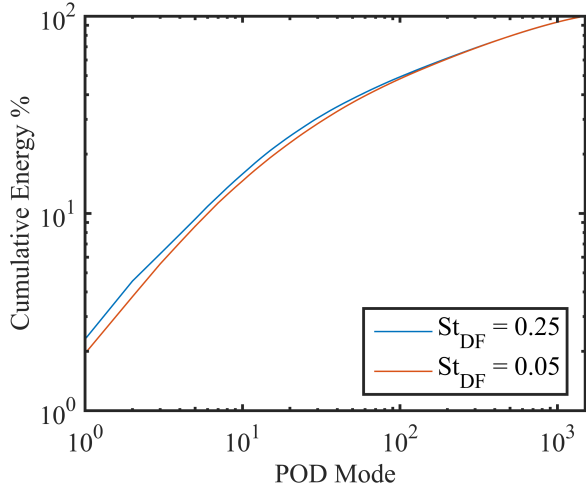


Figure 4.5: POD modal energy convergence.

2. Comparison of POD modes?

## 4.2 Large-Scale Structure Interactions

1. Merging of excited structures
2. Decay of LSS near end of potential core
3. Locally supersonic flow?

### 4.2.1 Global Flow-Field Effects

The global effects of excitation on shear layer development, both in general and in particular for LAFPAs, has been well-documented in the literature already (see Samimy *et al.* [? ] for a review on LAFPA excitation in jets). Therefore, only the features relevant to the current work will be briefly covered here. Excitation produces highly-energetic structures which entrain the ambient fluid surrounding the shear layer, thus increasing mixing between the high-momentum core fluid and the ambient

fluid. As a result, the growth rate of the shear layer can be amplified significantly; this is illustrated in Fig. 4.6. Excitation near the jet column mode ( $St \simeq 0.35$ ) produces a rapid spreading of the initial shear layer until  $x/D \simeq 5$ , after which the spreading rate returns to the natural spreading rate. (A quick note about the axial velocity fields shown in Fig. 4.6: the twelve circular regions of low velocity aligned on the outer edge of the lower shear layer are experimental artifacts. Laser reflections off of the microphones saturated the cameras, thus precluding the possibility of computing cross-correlations for these locations. Contrary to how it might appear in this figure, the microphone array is not in the flow-field, but situated behind from the cameras' point of view.)

The increased mixing also affects the high-velocity side of the shear layer, resulting in a reduction in the length of the potential core. In Fig. 4.7, the time-averaged centerline Mach number for each excitation case (as well as the natural jet) has been plotted as a function of axial distance. A slow progression in the location of the end of the potential core is clearly evident, with it shifting upstream from  $x/D \simeq 6$  eventually to  $x/D \simeq 5$  as the excitation Strouhal number nears the jet preferred frequency of  $St_{DF} \simeq 0.35$  (though not shown here, above this excitation frequency the effect is reduced). The location of the end of the potential core is of particular interest for the current work, as previous researchers have indicated that the dominant noise generation mechanism is associated with the violent breakdown of large-scale axisymmetric structures as they pass through the end of the potential core [? ] [reference ch3 here?].

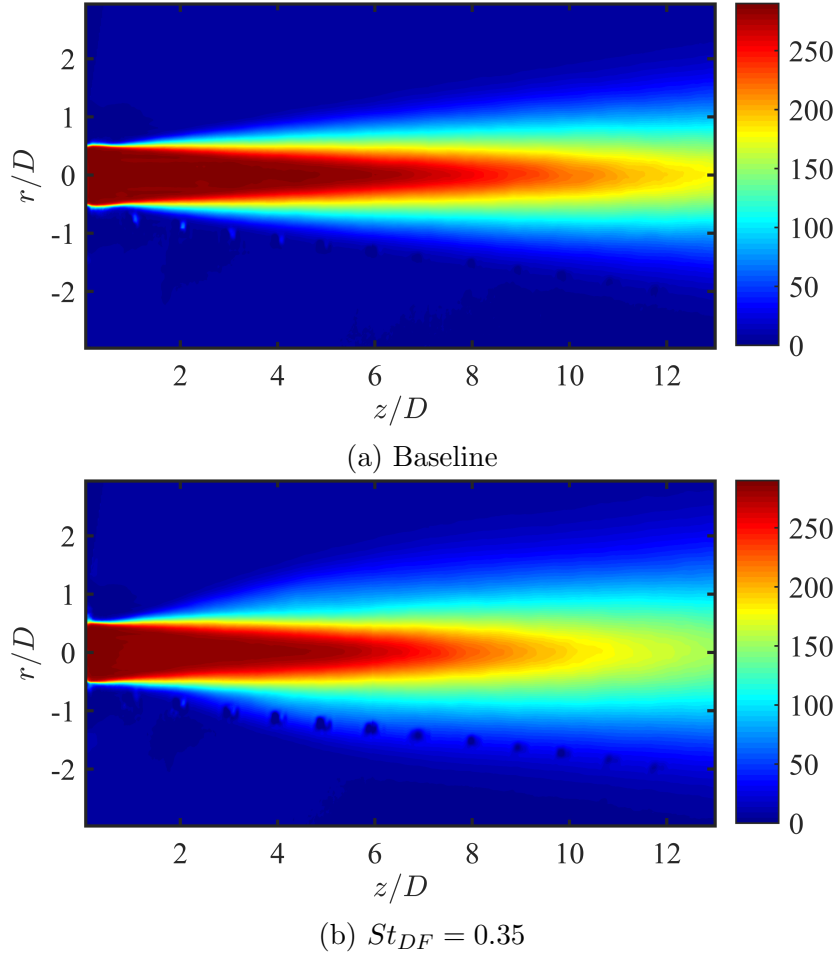


Figure 4.6: Effect of excitation on the shear layer spreading rate, as visualized by the axial component of the velocity field.

This breakdown occurs because as the shear layers merge, the interface between the interior sides of the ring vortex becomes highly unstable, so any small perturbations quickly grow and destroy the vortex. The exact location at which this breakdown occurs is ultimately going to be a function of structure growth rate, as larger structures will self-interact further upstream. The location of the end of the potential core is therefore dependent on the passage of the large-scale structures, and hence is not

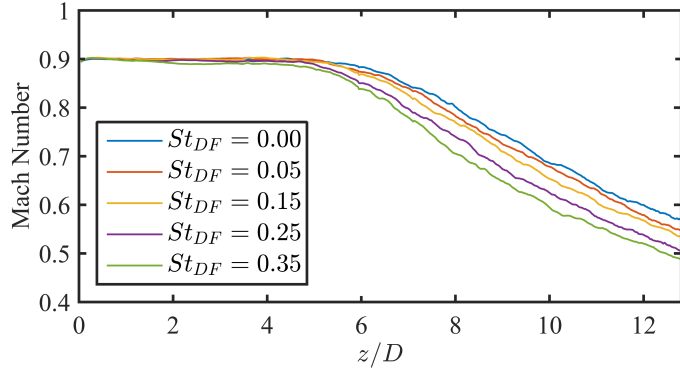


Figure 4.7: Centerline Mach number for all excitation cases; baseline jet is indicated by ‘0.00’.

strictly constant in time [who to cite here??]. Therefore, an axial shift in the time-averaged acoustic source is not necessarily reflective of a changing source mechanism, but may instead simply indicate that the source mechanism is now occurring at a different location.

## Chapter 5: Dilatation as the Aeroacoustic Source

Ribner presented an alternative approach to Lighthill's acoustic analogy which posited fluctuating fluid dilatations as the source of aeroacoustic emission [41]. This is a reinterpretation of Lighthill's source, which in subsonic, unheated, turbulent jets consists of fluctuating momentum flux. The driving factor behind Ribner's analysis is the conceptual simplification of the aeroacoustic sources: Lighthill's quadrupoles are replaced by the contraction or expansion of fluid elements (confusingly identified alternatively as *pseudosound* or *pseudo-pressure*) due to the fluctuating momentum flux, which in turn drive the acoustic field. This conceptual simplicity makes the dilatation-based approach to the acoustic analogy particularly attractive to the experimentalist for high-speed (though subsonic), turbulent flows. The analysis, described briefly in the subsequent section, is (relatively) simple to perform computationally, relying exclusively on second-order derivatives (unlike the third-order differential equation derived by Lilley [27]) which include a natural filtering mechanism. More importantly, the pseudosound field (which is the direct precursor to the source field) can be directly compared against the time-resolved hydrodynamic pressure field measured in the irrotational near-field, thus serving as a helpful validation of the computations.

## 5.1 Ribner's Acoustic Analogy

To briefly acquaint the reader, an overview of Ribner's analysis will be provided here. Further details can be found in Ribner [41] if the reader is so inclined. Ribner's analysis directly follows from Lighthill's, and as such includes the same restrictions on the applicable class of flows. Starting from Lighthill's analogy (Eqn. 1.2), the source term is first reduced by neglecting viscosity and entropic fluctuations (thereby assuming that the flow is of high Reynolds number and unheated), leaving only the Reynolds stress terms:

$$\frac{1}{c^2} \frac{\partial^2 p}{\partial t^2} - \nabla^2 p = \nabla \cdot \nabla \cdot \rho \mathbf{u} \otimes \mathbf{u}. \quad (5.1)$$

Ribner then split the pressure fluctuations into a propagative acoustic component and an incompressible component (pseudosound, which is associated with the convective hydrodynamic fluctuations),  $p' + p_0 = p_a + p_s$ . The incompressible component of the flow will then satisfy

$$\rho \frac{\partial}{\partial t} (\nabla \cdot \mathbf{v}) = 0 \quad (5.2)$$

where  $\mathbf{v}$  is now used in place of  $\mathbf{u}$  to signify an incompressible (solenoidal) velocity field. Therefore,

$$-\nabla^2 p_s = \nabla \cdot \nabla \cdot \rho_0 \mathbf{v} \otimes \mathbf{v}. \quad (5.3)$$

Ribner's analysis then assumes that the full density and velocity fields can be approximated as the incompressible (solenoidal) fields (the higher-order terms scaling with the *fluctuating* Mach number [42]), thus producing Ribner's Dilatation Equation

$$\frac{1}{c^2} \frac{\partial^2 p_a}{\partial t^2} - \nabla^2 p_a = -\frac{1}{c^2} \frac{\partial^2 p_s}{\partial t^2}. \quad (5.4)$$

In this way, acoustic pressure field is ultimately linked to the time rate of change of the dilatation (see Ristorcelli [42] for a very enlightening perturbation analysis which

makes this relationship far more clear). This is far from a controversial assertion; numerous other researchers have used the dilatation field to examine the aeroacoustic phenomena (primarily using DNS or LES simulations); see Mitchell *et al.* [cite 1995], Colonius *et al.* [cite 1997], or Freund *et al.* [cite 2000] for examples. In fact, this relationship can easily be illustrated, as has been done in Fig. 5.1. Here, phase-averaged data at two phases has been plotted from a simulated Mach 0.9 jet excited by plasma actuators at  $St_{DF} = 0.25$ ; details of the numerical methods and results can be found in Speth & Gaitonde [43]. The toroidal structures generated by the excitation have been visualized in the foreground using Q-criterion, and the dilatation field in the background in grayscale. Highly coherent dilatation waves can be observed convecting with the large-scale structures near the shear layer. Further out radially, the dilatation field becomes less coherent and more indicative of far-field propagating pressure waves. Broadly and qualitatively speaking, the connection between the large-scale structures and the acoustic emission is clear; the current work represents a timid attempt to evaluate this relationship more formally.

## 5.2 Numerical Methodology

Computing the aeroacoustic source per Ribner's dilatation method from the estimated, time-resolved velocity field constitutes a three-step process. First, the solenoidal velocity field is computed via the Helmholtz' decomposition; the double divergence of the resulting stress tensor is then used as the source of Poisson's equation to calculate the pseudo-pressure field. Finally, the pseudo-pressure field is filtered

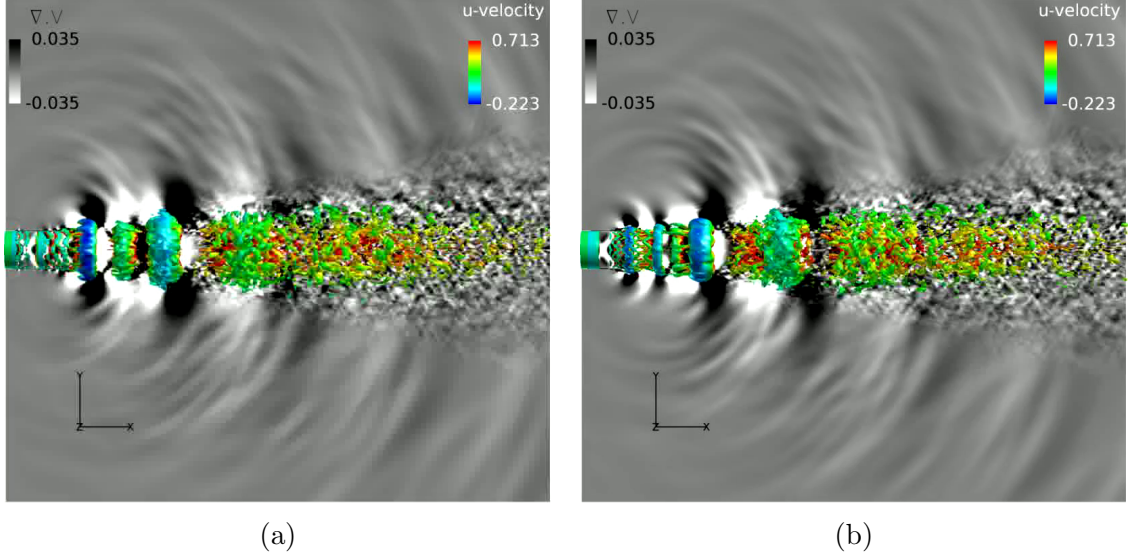


Figure 5.1: Two phases of actuation taken from the implicit LES database of Speth & Gaitonde [43]. Isosurfaces are computed from Q-criterion and colored by axial velocity, and the background corresponds to dilatation.

in time using an energy threshold in the wavelet domain, and the second time derivative of the resultant field is computed, producing the source field. This process is outlined in the following sections.

### Helmholtz Decomposition

For a given vector field,  $\mathbf{F}$ , Helmholtz's theorem states that any sufficiently smooth vector field can be linearly decomposed into irrotational and solenoidal vector fields, as

$$\mathbf{F} = \mathbf{F}_{potential} + \mathbf{F}_{rotational} = \nabla\Phi + \nabla \times \Psi \quad (5.5)$$

where  $\Phi$  is a scalar field and  $\Psi$  is a vector field. From basic vector calculus properties, one can therefore compute these solenoidal and irrotational components by taking the

divergence of this equation, leading to:

$$\nabla \cdot \mathbf{F} = \nabla^2 \Phi \quad (5.6)$$

which is simply Poisson's equation, where in the context of a velocity decomposition the forcing term is simply the divergence of the flow field (that is, the dilatation).

This initially presents a quandary for the researcher, as only planar PIV measurements are available, and hence the azimuthal velocity and derivative terms are unknown. As mentioned previously, the flow-field in a natural, high Reynolds number jet is a combination of numerous azimuthal Fourier modes. Though the velocity field has been found to contain a significant amount of energy at the higher order modes, the axisymmetric mode is still the dominant mode [44]. Additionally, it is the acoustic emission from the coherent large-scale toroidal structure generated by excitation that is the primary focus of this endeavor, not the full acoustic emission from the relatively incoherent natural turbulence. Due to the specific nature of the excitation (axisymmetric excitation), it is not expected that the azimuthal components of the flow is significant.

The database of Speth & Gaitonde [43] was provided to the author for the purpose of validating this assumption. Comparisons between the near-field pressure response to excitation of the experimental (§3) and numerical databases were performed in the reference, and a good match was found. Sample results for the pressure and radial velocity field for a single azimuthal plane are shown in Fig. 5.2; these results correspond to an actuation phase of  $1.4\pi$  for  $St_{DF} = 0.05$ , and have been phase-averaged over nine actuation cycles. (While less than desirable, the simulationists could not store the full, instantaneous 3-D velocity fields due to harddrive limitations. The  $St_{DF} = 0.05$  was therefore chosen for this analysis since it contained the fewest

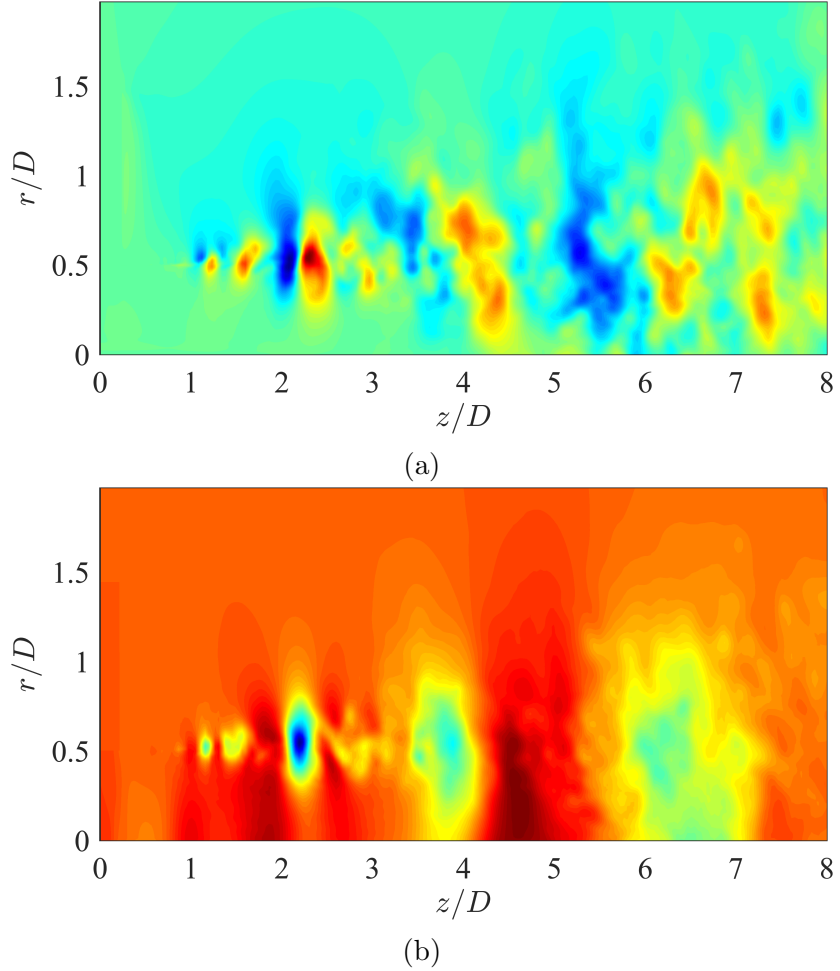


Figure 5.2: Streamwise velocity (a) and pressure (b) contours taken from the database of Speth & Gaitonde [43] for  $St_{DF} = 0.05$ .

number of actuation cycles and thus has the highest level of incoherent fluctuations.)

From these plots, a large-scale coherent structure generated by the excitation can easily be identified, centered at  $z/D = 2.1, r/D = 0.5$ .

The azimuthal velocity field corresponding to the axial location of the large-scale structure is shown in Fig. 5.3. While the azimuthal velocity is, unsurprisingly, non-zero, the field is highly incoherent as compared to the radial or axial velocity fields

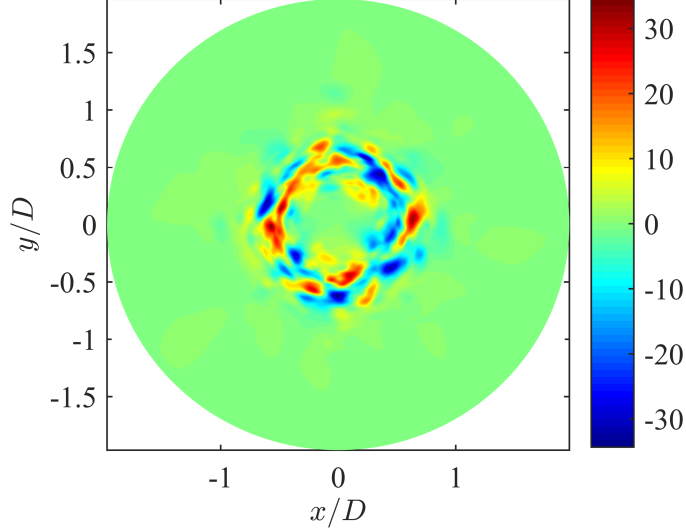


Figure 5.3: Azimuthal velocity at  $z/D = 2.1$  for the same instance as the previous figure; units are in m/s.

and of much lower amplitude. Finally, The dilatation field computed using the full 3-D gradients and the partial dilatation field computed using only the radial and axial gradients can be found in Fig. 5.4. Because there are weak azimuthal structures inherent even in the excited turbulent jet, a noticeable difference between the two- and full three-component dilatation fields is readily apparent in terms of fluctuation amplitude. However, the spatial structure of the full dilatation field is largely retained in the reduced (two-component) dilatation field, just at an amplitude reduced by a nearly constant factor of  $\sim 2$ . Because of this, the loss of the azimuthal gradient information is not expected to be produce unacceptable errors in the final solution. Therefore, the azimuthal terms are dropped, leaving

$$\frac{\partial U_r}{\partial r} + \frac{\partial U_z}{\partial z} + \frac{U_r}{r} = \frac{1}{r} \frac{\partial \Phi}{\partial r} + \frac{\partial^2 \Phi}{\partial r^2} + \frac{\partial^2 \Phi}{\partial z^2}. \quad (5.7)$$

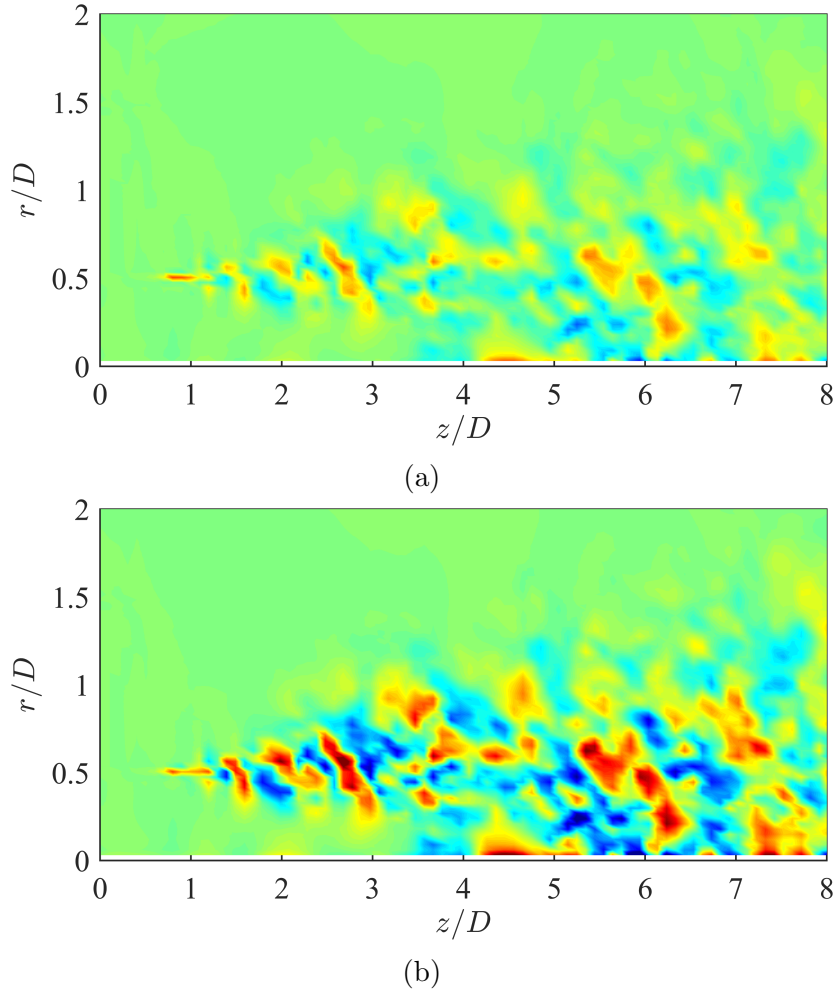


Figure 5.4: Dilatation computed using only the axial and radial components (a) and computed using the full three-component velocity vector; a uniform colorscale has been used for the two plots.

The solution procedure is therefore to first compute  $\Phi$  using Eqn. 5.7, then subtract the gradient of this field (the potential velocity field) from the raw velocity vector field in order to produce the solenoidal velocity field. This was done using a standard, second-order accurate centered finite difference scheme by Taylor approximation. A relatively low-order approximation to the spatial derivatives was deemed

sufficient for this particular work, as the spatial grid was very fine compared to the wavelength of the dominant structures under investigation. For reference,  $ds = 0.6$  mm and therefore  $l/ds \simeq 30$ , where  $l$  is the average characteristic length of the excited large-scale structures near the end of the potential core and  $ds$  is the grid spacing.

As the flow has already been assumed to be axisymmetric, the Poisson equation is solved over the top half of the jet only. (The top plane was chosen as the microphone tips are visible in the lower plane, which produced spurious vectors in the shear layer.) At the lower boundary (jet centerline), a zero-normal-gradient boundary condition was used to enforce axisymmetry. At the radial boundary, the solenoidal component was set to zero (as there is no turbulent flow in this region, and the only outgoing waves will be compressible). At the inflow and outflow however, the proper boundary conditions are not immediately obvious. Other researchers using numerical databases [45] have argued that the solenoidal component be set to zero here as the turbulent eddies have either not grown to significant values or decay to insignificant values at these locations, respectively. For the domain explored in the current work however, this does not appear to be necessarily accurate. At the outflow boundary ( $z/D \simeq 13$ ), there is still significant vortical behavior, but the Mach number is relatively low ( $M_j \sim 0.5$ ) and hence compressibility is expected to be negligible. For the domain explored in the current work however, this does not appear to be necessarily accurate, and instead the *potential* component is set to zero at both the inlet and outlet. At the outflow boundary ( $z/D \simeq 13$ ), there is still significant vortical behavior, but the Mach number is relatively low ( $M_j \simeq 0.5$ ) and hence compressibility is expected to be negligible. At the inflow boundary (which is  $\sim 1.4$  mm downstream of the nozzle exit), the solenoidal component is clearly not negligible in the shear layer region (since  $\partial U_z / \partial r \neq 0$ ). If

the inflow is approximated as a plug flow (which the ensemble-averaged PIV indicates is not an unreasonable assumption),  $\partial U_z / \partial z = \partial U_r / \partial r = 0$  and hence the potential component is negligible here. Therefore, the potential component was set to zero at both the inlet and outlet. Second-order accurate centered finite differences were again used to approximate the derivatives in the boundary conditions; a single ghost node was along each boundary to enforce these conditions.

Sample results for this procedure have been provided in Fig. 5.5. Here, the axial and radial velocity components for the original (estimated) and decomposed velocity fields are shown for  $St_{DF} = 0.05$ . From the raw velocity field, a single large-scale structure is readily identifiable at  $z/D \simeq 6$  (which is the end of the potential core). Due to the very low frequency of the excitation (impulsive forcing), no other large-scale structures are clearly visible in the flow-field. As expected, the Helmholtz decomposition produces a solenoidal velocity that is quite similar to the full velocity field; even at high subsonic Mach numbers, compressibility plays a minor (though definitely non-negligible) role in the overall evolution of the shear layer and potential core. The potential (compressible) velocity field does exhibit coherent axial and radial velocity fluctuations which correspond to the large-scale structure; in fact, the potential and solenoidal velocity fluctuations associated with the large-scale structure are of similar magnitude, suggesting that compressibility is important for the development of the large-scale structure themselves.

The upstream development of the potential field, in which no large-amplitude oscillations are observed, validates the assumption of plug flow made in the boundary conditions. In contrast, non-negligible fluctuations are observed near the outflow boundary; unfortunately, the experimental domain does not extend far enough

downstream for the compressible component to fully decay. However, the potential component is still far weaker than the solenoidal component. For validation purposes, the boundary conditions of [Unnikrishnan2015,Mansour] (zero solenoidal component at the inflow and outflow) were also implemented and compared against the current results. Though not shown here for brevity, the zero-solenoidal boundary conditions produced similar fields at the interior of the domain, but non-physical oscillations at the inflow and outflow boundaries. Based on these results, the zero-potential boundary conditions were retained; though there is a discrepancy between the boundary conditions and the physical system at the outflow boundary, the numerical effects of this are expected to be minor.

### Pseudo-Pressure Solver

Once the solenoidal velocity field is known, the fluctuating pseudo-sound field can be computed as the incompressible solution to the momentum and continuity equations (Eqn. 5.3). The source field is calculated explicitly from the solution of the Helmholtz decomposition (that is, the double divergence of the incompressible velocity stress tensor) using second-order accurate finite differences. As with the preceding Poisson equation, the azimuthal terms in this second Poisson equation are assumed negligible in comparison to the radial and axial terms and are thus ignored. Again, as done previously for the Helmholtz decomposition, the governing equation is approximated using second-order accurate centered finite differences, and ghost nodes are used at the domain boundaries to enforce the boundary conditions.

The hydrodynamic pressure field has been observed to strongly decay with radial position [46]; given the radial extent of the experimental domain, it was therefore assumed that the pseudo-sound fluctuations have decayed to negligible values by

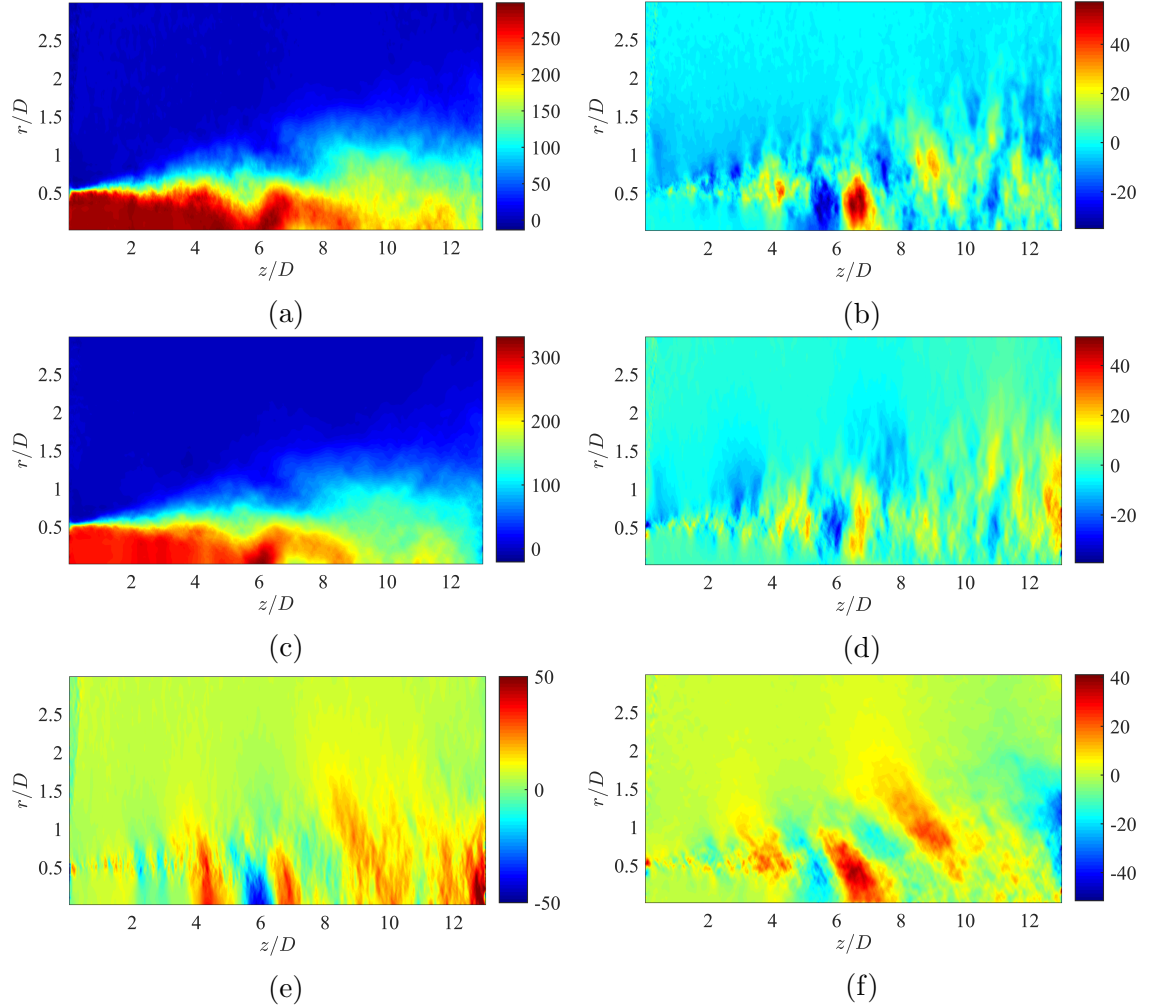


Figure 5.5: Instantaneous axial (a,c,e) and radial (b,d,f) velocity components for the original (a,b), solenoidal (c,d), and potential (e,f) velocity fields (units in m/s), for  $St_{DF} = 0.05$ .

the time they reach the upper domain boundary. In accordance with the boundary assumptions made in the preceding section, at the inflow boundary plug flow has again been assumed, meaning that the pseudo-pressure *fluctuations* are negligible at the inlet. The outflow boundary was assumed to be far enough downstream such

that the fluctuations were also negligible at the boundary. Finally, the lower boundary enforced the zero-normal-gradient required by the assumption of axisymmetry.

Sample results for the pseudo-pressure field are shown in Fig. 5.6, which corresponds to the solenoidal velocity decomposed in Fig. 5.5. As expected, a spatially-coherent fluctuation is observed coinciding with the location of the large-scale structure as identified in the velocity field. Lower-amplitude oscillations are also observed upstream of the end of the potential core, while downstream the fluctuations are fairly incoherent and low-amplitude. By the end of the experimental domain, the pseudo-pressure field has decayed to essentially negligible values. At the inlet however, a large-amplitude pressure sink resides along the jet lipline and extends for  $z/D \lesssim 0.5$ . The origin of this pressure sink is not clear to the research, however it is entirely numerical in nature; as will be seen in the following section, the consistency of this sink results in no superfluous aeroacoustic source being computed for this location. While the presence of this numerical error is unfortunate, given that it was found to not have a major effect on the computed aeroacoustic source field (which is ultimately the goal of this analysis), further inquiry into the cause of this numerical error was deemed unproductive.

## Wavelet Denoising and Source Computation

The aeroacoustic source term can now be computed explicitly as the second temporal derivative of the pseudo-sound field (Eqn. 5.4). However, filtering of the pseudo-pressure field along the temporal dimension was found to be necessary before computation of the derivative, due to the accumulation of experimental and numerical error. As discussed by Farge [47], unlike the Fourier transform coefficients which are well-localized in frequency but completely delocalized in time, the wavelet transform

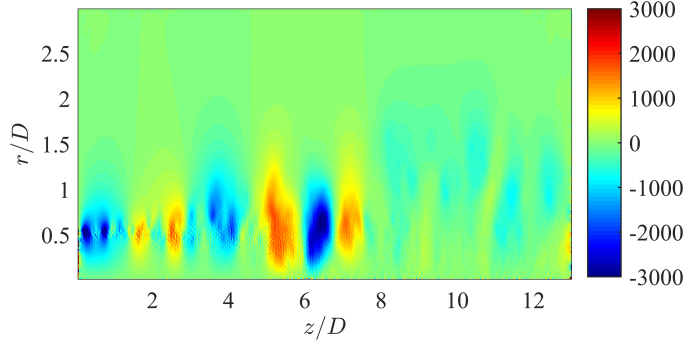


Figure 5.6: Instantaneous pseudo-pressure field for the same conditions as Fig. 5.5.

coefficients are well-localized in both frequency and time. As a result, a truncated set of the wavelet coefficients will better preserve the temporal characteristics of a given signal than a truncated set of Fourier coefficients. Hence, wavelet-based filtering was used to remove the influence of the experimental/numerical errors; more specifically, an energy threshold was applied to the orthogonal wavelet coefficients in order to remove the less-energetic, incoherent events from the pseudo-pressure field. Interested readers should see Donoho & Johnstone [1994], Farge *et al.* [1999] and Ruppert-Felsot *et al.* [2009] for additional details on denoising using orthogonal wavelet transforms, including more advanced algorithms.

For the current work, the fast orthogonal wavelet transforms implemented in Stanford University, Department of Statistics' WaveLab 850 software library were utilized. The mother wavelet was defined as the 5<sup>th</sup>-order Battle-Lemarie wavelet; sample data was also analyzed using other smooth wavelets (high-order Coiflets and Symmlets) to ensure that the final results were not affected by the choice of mother wavelet. The orthogonal wavelet transform was performed along the temporal domain separately for each spatial location; the time-series was zero-padded so that it matched a dyadic

grid. A soft energy threshold was used to separate the coherent, large-scale pressure fluctuations from the incoherent noise. In traditional wavelet-denoising, the threshold is often defined as  $\epsilon = \sqrt{2\sigma_n^2 \log_e N}$ , where  $\sigma_n^2$  is the variance of the noise, and  $N$  is the sample length. However, for the current work this threshold was found to be too lax, and so a much more aggressive energy threshold was used.

In the work of Kearney-Fischer *et al.* [cite], a pseudo-wavelet filter was used on the far-field signal at aft angles in order to extract the dominant, intermittent acoustic events which were believed to be related to the dominant, intermittent large-scale structures in the jet shear layer. In that work, an energy cutoff of  $\epsilon = 1.5\sigma$  was used; here  $\sigma^2$  corresponds instead to the variance of the *signal* rather than the noise in the signal. Kearney-Fischer *et al.* found that a signal filtered in such a manner retained the relevant aspects of the far-field acoustic spectrum at shallow angles, in particular the dominant energy peak and strong roll-off at high and low frequencies. Based on these results, a threshold of  $\epsilon = 2\sigma$  was chosen for the current work (due to the low signal-to-noise ratio); for consistency,  $\sigma$  was calculated over the entire field rather than at each individual point; the error (and hence, energy) did not scale with spatial location, resulting much lower signal-to-noise ratios at far radial and axial positions.

Sample results for the wavelet-denoising are shown in Fig. 5.7 for  $z/D = 1.75$  at the jet lipline (as will be shown later, the sources are centered around the jet lipline upstream of the end of the potential core). A high-amplitude, relatively low-frequency compact waveform is observed in the pseudo-pressure field centered around  $\tau U_j/D \simeq 2.25$ ; this is the hydrodynamic wave associated with the passage of the large-scale structure observed in Fig. 5.5. While intuitively one would expect the temporal derivative of this compact waveform to dominate the source field, without

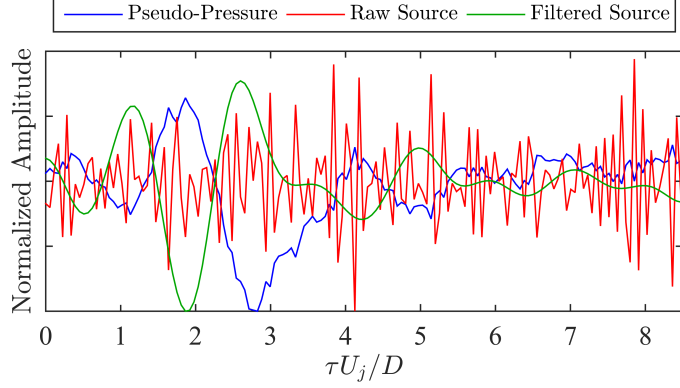


Figure 5.7: Effects of filtering of the pseudo-pressure field on the calculated aeroacoustic source at  $z/D = 1.75, r/D = 0.5$ ; amplitudes have been arbitrarily normalized to ease visual comparisons.

filtering the source field is completely dominated instead by the high-frequency noise in the pseudo-pressure even though it is of comparably low amplitude. The wavelet-denoising eliminates this error however, and recovers the expected behavior for the second temporal derivative.

Once the pseudo-pressure field has been properly filtered, the aeroacoustic source is simply calculated using second-order finite differences in time (Fig. 5.7). To compute the far-field noise, the source field can be spatially-integrated in retarded time, accounting for the propagation delay from each source location to the observer, per Eqn. 1.5; here, this was performed by trapezoidal integration.

### 5.3 Wavepackets in the Pseudo-Pressure Field

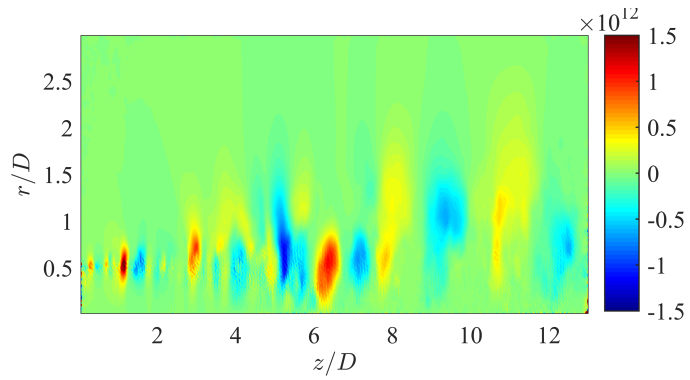


Figure 5.8: Instantaneous source field for the same conditions as Fig. 5.5.

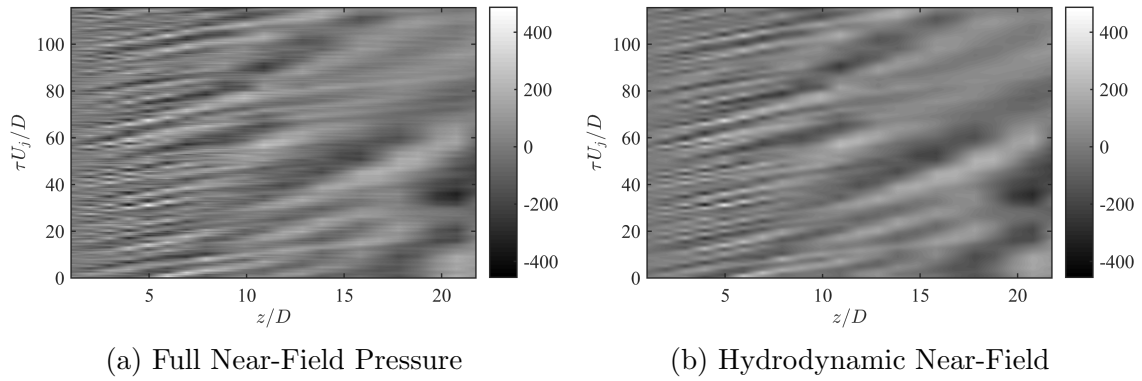


Figure 5.9: ???

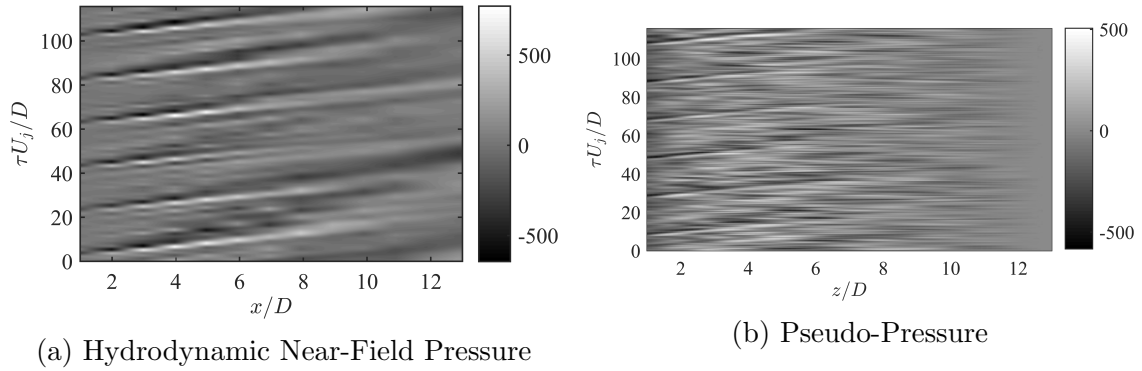


Figure 5.10: ???

## **Chapter 6: Conclusions**

## Bibliography

- [1] Christopher K. W. Tam, Golebiowski, Michel, and J. M. Seiner. On the two components of turbulent mixing noise from supersonic jets. In *2nd AIAA/CEAS Aeroacoustics Conference*, number 1996-1716, 1996.
- [2] K Viswanathan. Scaling laws and a method for identifying components of jet noise. *AIAA Journal*, 44(10):2274–2285, 2006.
- [3] Christopher K. W. Tam, K. Viswanathan, K. Ahuja, and J. Panda. The source of jet noise: Experimental evidence. *Journal of Fluid Mechanics*, 615:253–292, 2008.
- [4] Marie Cabana, Vronique Fortun, and Peter Jordan. Identifying the radiating core of lighthill’s source term. *Theoretical Computational Fluid Dynamics*, 22: 87–106, 2008.
- [5] P. Jordan and Y. Gervais. Subsonic jet aeroacoustics: associating experiment, modelling and simulations. *Experiments in Fluids*, 44:1–21, 2008.
- [6] M. Wei and J. B. Freund. A noise-controlled free shear flow. *Journal of Fluid Mechanics*, 546:123–152, 2006.

- [7] André V. G. Cavalieri, P. Jordan, Yves Gervais, and A. Agarwal. Jittering wave-packet models for subsonic jet noise. In *16{th AIAA/CEAS Aeroacoustics Conference*, number 2010–3957, Stockholm, Sweden, June 7–9 2010.
- [8] James Bridges and Clifford A. Brown. Parametric testing of chevrons on single flow hot jets. In *10<sup>th</sup> AIAA/CEAS Aeroacoustics Conference*, number 2004–2824, Manchester, United Kingdom, May 10–12 2004.
- [9] M. Samimy, K. B. M. Q. Zaman, and M. F. Reeder. Effect of tabs on the flow and noise field of an axisymmetric jet. *AIAA Journal*, 31(4):609–619, 1993.
- [10] Yurii G. Utkin, Saurabh Keshav, Jin-Hwa Kim, Jeff Kastner, Igor V. Adamovich, and Mo Samimy. Development and use of localized arc filament plasma actuators for high-speed flow control. *Journal of Physics D: Applied Physics*, 40(3):685–694, 2007.
- [11] M. Samimy, J. H. Kim, J. Kastner, I. Adamovich, and Y. Utkin. Active control of a mach 0.9 jet for noise mitigation using plasma actuators. *AIAA Journal*, 45(4):890–901, 2007.
- [12] M. Samimy, J. H. Kim, J. Kastner, I. Adamovich, and Y. Utkin. Active control of high-speed and high-reynolds-number jets using plasma actuators. *Journal of Fluid Mechanics*, 578(1):305–330, 2007.
- [13] M. Samimy, J.-H. Kim, M. Kearney-Fischer, and A. Sinha. Acoustic and flow fields of an excited high reynolds number axisymmetric supersonic jet. *Journal of Fluid Mechanics*, 656:507–529, 2010.

- [14] J.-H. Kim, M. Kearney-Fischer, M. Samimy, and S. Gogineni. Far-field noise control in supersonic jets using conical and contoured nozzles. *ASME Journal of Engineering for Gas Turbine and Power*, 133:081201, 2011.
- [15] Jin-Hwa Kim and Mo Samimy. Effects of active control on the flow structure in a high reynolds number supersonic jet. *International Journal of Flow Control*, 1(2):99–117, 2009.
- [16] M. Kearney-Fischer, J.-H. Kim, and M. Samimy. Control of a high reynolds number mach 0.9 heated jet using plasma actuators. *Physics of Fluids*, 21:095101, 2009.
- [17] M. Kearney-Fischer, J.-H. Kim, and M. Samimy. A study of mach wave radiation using active control. *Journal of Fluid Mechanics*, 681:261–292, 2011.
- [18] Alfons Michalke. Survey on jet instability theory. *Progress in Aerospace Sciences*, 21:159–199, 1984.
- [19] J. Cohen and I. Wygnanski. The evolution of instabilities in the axisymmetric jet. part 1 the linear growth of disturbances near nozzle. *Journal of Fluid Mechanics*, 176:191–219, 1987.
- [20] S. C. Crow and F. H. Champagne. Orderly structure in jet turbulences. *Journal of Fluid Mechanics*, 48(3):547–591, 1971.
- [21] G. L. Brown and A. Roshko. On density effects and large structure in turbulent mixing layers. *Journal of Fluid Mechanics*, 64(4):775–816, 1974.
- [22] Valdis Kibens. Discrete noise spectrum generated by an acoustically excited jet. *AIAA Journal*, 18(4):434–441, 1980.

- [23] R. A. Petersen and M. M. Samet. On the preferred mode of jet instability. *Journal of Fluid Mechanics*, 194:153–173, 1988.
- [24] M. J. Lighthill. On sound generated aerodynamically. i. general theory. In *Proceedings of the Royal Society of London: Series A, Mathematical and Physical Sciences*, volume 211, pages 564–587. The Royal Society, 1952.
- [25] D. G. Crighton, A. P. Dowling, J. E. Ffowcs Williams, M. Heckl, and F. G. Leppington. *Modern Methods in Analytical Acoustics*. Springer-Verlag, 2nd edition, 1992.
- [26] M. Goldstein. *Aeroacoustics*. NASA Scientific and Technical Information Office, 1974.
- [27] Geoffrey M. Lilley. The source of aerodynamic noise. *International Journal of Aeroacoustics*, 2(3):241–254, 2003.
- [28] Alan Powell. Theory of vortex sound. *Journal of the Acoustical Society of America*, 36(1):177–195, 1964.
- [29] P. E. Doak. Momentum potential theory of energy flux carried by momentum fluctuations. *Journal of Sound and Vibration*, 131(1):67–90, 1989.
- [30] M. J. Lighthill. On sound generated aerodynamically ii. turbulence as a source of sound. *Proceedings of the Royal Society of London. Series A, Mathematical and Physical Sciences*, 222(1148):1–32, 1954.
- [31] Erik Mollo-Christensen. Jet noise and shear flow instability seen from an experimenter’s viewpoint. *ASME Journal of Applied Mechanics*, 34:1–7, 1967.

- [32] A. Michalke. On spatially growing disturbances in an inviscid shear layer. *Journal of Fluid Mechanics*, 23(3):521–544, 1965.
- [33] Christopher K. W. Tam, K. Viswanathan, K. Ahuja, and J. Panda. The source of jet noise: Experimental evidence. *Journal of Fluid Mechanics*, 615:253–292, 2008.
- [34] J. Panda, R. G. Seasholtz, and K. A. Elam. Investigation of noise sources in high-speed jets via correlation measurements. *Journal of Fluid Mechanics*, 537:349–385, 2005.
- [35] K. Viswanathan. Distributions of noise sources in heated and cold jets: are they different? *International Journal of Aeroacoustics*, 9(4 & 5):589–626, 2010.
- [36] C. Bogey and C. Bailly. An analysis of the correlations between the turbulent flow and the sound pressure fields of subsonic jets. *Journal of Fluid Mechanics*, 583:71–97, 2007.
- [37] Christopher K. W. Tam. Supersonic jet noise. *Annual Review of Fluid Mechanics*, 27:17–43, 1995.
- [38] Dominik Obrist. Acoustic emissions from convected wave packets. *Physics of Fluids*, 23:026101, 2011.
- [39] André V. G. Cavalieri, Daniel Rodriguez, Peter Jordan, Tim Colonius, and Yves Gervais. Wavepackets in the velocity field of turbulent jets. *Journal of Fluid Mechanics*, 730:559–592, 2013.
- [40] Y. Baqui, A. Agarwal, and A. Cavalieri. A coherence-matched linear model for subsonic jet noise. Number 2014-2758, 2014-08-18 2014.

- [41] H. S. Ribner. Aerodynamic sound from fluid dilatations. UTIA Report 86, Institute of Aerophysics, University of Toronto, 1962.
- [42] J. R. Ristorcelli. Fluctuating dilatation rate as an acoustic source. ICASE Report 97-21, NASA Langley Research Center, Hampton, Virginia, 1997.
- [43] Rachelle L. Speth and Datta V. Gaitonde. Near field pressure and associated coherent structures of excited jets. In *Proceedings of ASME 2014 Fluids Engineering Division Summer Meeting*, number FEDSM2014-21186, Chicago, Illinois, August 3–7 2014.
- [44] Mark N. Glauser and William K. George. Orthogonal decomposition of the axisymmetric jet mixing layer including azimuthal dependence. *Advances in Turbulence*, pages 357–366, 1987.
- [45] S. Unnikrishnan and Datta V. Gaitonde. Acoustic, thermal and turbulent modes in a supersonic cold jet. *Submitted to the Journal of Sound and Vibration*, 2015.
- [46] R. E. A. Arndt, D. F. Long, and M. N. Glauser. The proper orthogonal decomposition of pressure fluctuations surrounding a turbulent jet. *Journal of Fluid Mechanics*, 340:1–33, 1997.
- [47] Marie Farge. Wavelet transforms and their applications to turbulence. *Annual Review of Fluid Mechanics*, 24:395–457, 1992.